# UNIVERSITÀ DEGLI STUDI DI NAPOLI FEDERICO II

## DOTTORATO DI RICERCA IN

## TECNOLOGIE INNOVATIVE PER MATERIALI SENSORI ED IMAGING

## XVIII CICLO

# Chemical vapor deposition of carbon nanotubes on iron-patterned substrates:
# towards a control of the positioning and structure

Ph.D Thesis of

## MARIA FORTUNA BEVILACQUA

**Tutor interno:**

Prof. Ruggero Vaglio

**Tutor esterni:**

Dr. Rita Rizzoli

Dr. Vincenzo Vinciguerra

Napoli, Dicembre, 2005

# Contents

## *Introduction*

The discovery of the buckminsterfullerene $C_{60}$ in the mid-eighties (H. W. Kroto, R. F. Curl and R. E. Smalley), has polarized and triggered the interest of the scientific community on a novel and stable carbon allotropic form. As a direct consequence of all this research activity, in 1991  another stable class of fullerene type molecules was discovered by Iijima, during the exploitation of experiments for the arc-discharge synthesis of fullerene $C_{60}$. This new kind of a fullerene-like material was the Multi Wall Carbon Nanotubes (MWNTs). MWNTs are made of coaxial hollow cylinders with walls arising from the wrapping of single graphite layers. Their diameters range from 10 to 50 nanometers, whereas their lengths are different order of magnitude (micrometric or even millimetric scale) larger. The existence of carbon nanotubes made of a single wrapped up graphene layer (SWNTs, Single Wall Carbon Nanotubes), was proved by the same group two years later. The SWNTs are the most simple and ultimate structure that can be obtained nowadays, being formed by only one rolled graphene sheet.

The first studies on the properties of carbon nanotubes disclosed their extraordinary potentialities that are strictly determined by their quasi one-dimensional structure. In particular, a great breakthrough was achieved in 1997 when it was shown that the semiconducting SWNTs can be employed as the channel of a field effect transistor. As a consequence an enormous interest on the fullerene-like carbon nanotube materials arose due to different reasons:

The first one is the possibility of designing a material, suitable for specific applications in the field of electronic devices, by exploiting the intimate relation between its structural and electronic properties.

The second reason is the availability of a material that can be either a metal or a direct band gap semiconductor, whose nanometric dimensions define the scaling characteristic of the device.

The third is determined by the wide compatibility of CNTs with microelectronic applications, according to the new bottom-up approach for device implementations.

In fact, the ultra large scale integration process that is today employed within the standard electronic silicon-based technology, is rapidly approaching its physical limits (e.g. quantistic effects connected with the size reduction of electronic components) as well as its technological limits (e.g. the resolution of optical lithography), establishing

the maximum concentration of integrated CMOS devices in a density of $10^7$ devices/cm$^2$. Therefore, the empiric observation, also known as Moore's law, according to which the number of transistors implemented on a single circuit can double every 18-24 months doubling, at the same time, the rate of calculus, could not be further satisfied by using traditional materials. All these elements explain the increasing interest for the study and development of techniques for carbon nanotubes synthesis, allowing to move from a curiosity-driven to a commercially applicable research. The perspective of being able to modulate the electronic properties of CNTs, in order to replace traditional silicon-based electronic devices, for example by fabricating field effect transistors with carbon nanotubes as a channel for the charge transport (CNT-FET), is extremely interesting.

The final goal of designing all organic devices has to go through the intermediate step of the integration in silicon-based technologies. Therefore devices actually using Carbon Nanotubes are based on a hybrid technology.

In the case of CNT-based devices, the key point that has strongly limited the achievement of the maturity needed for the integration in commercial devices, is the still lacking control over the synthesis phase. In other words, this lack of control is the unavailability of deposition processes enabling the control of the CNTs in terms of localization, morphology and electronic properties, nonetheless being processes at low cost, reproducible and easily duplicable on an industrial scale.

Among the implemented methods for the nanotubes synthesis (the laser ablation, arc discharge and chemical vapor deposition), the catalytic process of chemical vapor deposition (CCVD) is the most widely used for several reasons: the scalability, its wide versatility, the possibility to achieve a strict control on the growth acting on the system configuration to implement deposition processes at very low temperatures, even at room temperature.

This thesis work will give a summary of the results of catalytic chemical vapor depositions experiments, developed for the growth of carbon nanotubes. In particular, we focused the thesis on different and consequential activities:

– the setting of CCVD processes for the controlled synthesis of carbon nanotubes by tuning the key parameters for switching from a particular kind of growth to another (second chapter);

− the analysis of morphological and structural properties of as-grown carbon nanotubes belonging to the different synthesis groups we implemented, providing a constant feedback on the growth process (fourth chapter);

− the investigation of feasible applications of carbon nanotubes in fields of interest for the industry (sixth chapter).

More precisely, in the first chapter the structural properties of carbon nanotubes, as well as the expressions for the energy dispersion relations, are reported. These have been obtained by applying the tight binding method to the hexagonal structure defining the graphite lattice. From the energy dispersion relations of bidimensional graphite, the energy dispersion relations of achiral carbon nanotubes in the zone-folding approximation have been obtained. The band structure of the graphite and of particular semiconducting (zig-zag (4,0)) and metallic (zig-zag (3,0), armchair (3,3)) carbon nanotubes, have been plotted, implementing a simple software calculation with MatLab.

In the second Chapter, in the specific, the results inherent the different kinds of growth implemented are reported. This is intended to demonstrate as the exact control of the synthesis parameters influencing the growth, allows to gain an increasing control on the orientation, density, localization, morphology and structure of as-grown nanotubes. These achievements fulfill the requirements of devices in which morphological and structural properties are completely addressed by the control of the synthesis process. These processes are required to be completely reproducible through the set up of the main parameters regulating the growth (as substrate, catalyst, process parameters, feedstock gases).

Four nanotubes classes, completely distinguished for their growth characteristics as well as properties, have been individuated. In this chapter it is demonstrated that the ability to switch from a vertical, highly dense growth of randomly bridging nanotubes to well located, well oriented, thin, bridging nanotubes on surfaces free from carbonaceous deposit, has been completely acquired. Therefore, the purpose to set up a reproducible process for the growth of single and well located nanotubes as well as of a network of nanotubes connecting two electrodes, on the way to manufacture a CNT-based device, has been almost completely achieved.

The third chapter provides very simple theoretical elements to analyze and understand the main carbon nanotubes characterization techniques, deeply described in the next chapter. In particular, in the fourth chapter the more representative results arising from the characterization techniques of carbon nanotubes, are presented and discussed. This allows to demonstrate the correlations between the different synthesis processes and the characteristics of the grown carbon nanotubes. Raman Spectroscopy is the key tool towards the understanding of CNTs structure and it has been discussed in details analyzing the possibility to check the presence of carbon nanotubes, their crystalline order and diameter, as well as the particular kind (SWNTs or MWNTs). The HRTEM and the EELS (Electron Energy Loss Spectroscopy) techniques have been hence used to check the morphology of the samples and to find the Fe inclusions inside the as-grown samples by means of chemical maps. Finally, a complete characterization is achieved by performing the AFM measurements on the most representative samples.

In the fifth chapter, two of the models proposed in the literature to explain the different kinds of nucleation and growth of carbon nanotubes are analyzed in details. Particular attention has been devoted in order to explain, within these theoretical models, the growth processes we observed. We highlighted common points and differences between proposed theoretical models and our experimental results. These discrepancies emphasized the uncertainties which are still present in the formulation of a definitive model, suitable to explain the phenomena regulating nanotubes nucleation and growth.

The sixth chapter represents a rapid excursus about potential applications of carbon nanotubes, referring in particular to the steps we moved towards the manufacturing of CNT-based FET. A very simple experiment is also described aiming at obtaining a nanocomposite material, made of CNTs and polymer. This is useful for the analysis of the modifications of the insulating behavior of a polystyrene matrix, whose conductivity increases after the addition of carbon nanotubes.

## *1.    Introduction*

Carbon is the sixth element (atomic number $Z = 6$) in the periodic table and the first element of the 4th group. Although carbon is positioned above silicon, the main element employed in the semiconductor industry, its properties are quite different from that of silicon. In fact, differently from silicon, elemental carbon has allotropes: the diamond and the graphite form. Diamonds and graphite are the two main allotropic forms of bulk carbon Fullerenes and carbon nanotubes can be considered as new allotropes that can occur in the nanostructured form of graphene sheets.

### *1.1   Graphite*

Graphite is the principal allotrope of carbon. The crystal structure of graphite consists of layers of carbon atoms arranged in a honeycomb or hexagonal network where the planes are stacked in an ABA arrangement. This means that A and B atoms of two consecutive layers are displaced at a certain distance in such a way that a C-atom results on the top of one of the ring of the honeycomb network. The in-plane nearest-neighbor distance $a_{cc}$ is 1.421 Å and the in-plane lattice constant $a_0$ is 2.462 Å, whereas the $c$-axis constant is $c_0 = 6.708$ Å connected with an interplanar distance of $c_0/2 = 3.3539$ Å.

The most used commercial graphite is the Highly Oriented Pyrolytic Graphite (HOPG) which is synthesized by the pyrolysis of hydrocarbons at a temperature above 2000 °C and then annealed above 3300 °C. HOPG shows electronic, transport, thermal and mechanical properties that are very close to that of an ideal single crystal of graphite with a high $c$-axis degree of alignment. The order degree of the as-produced HOPG is about 1 μm within the planes and 0.1 μm along the $c$-direction. The graphene parallel planes of HOPG form a sufficiently ordered structure that can be used commercially as a monochromator crystal for X-ray and neutron diffraction [1].
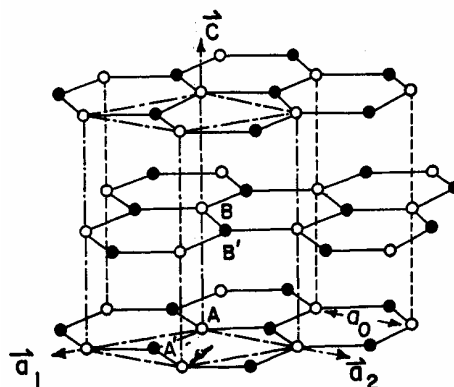
**Fig. 1.1.1**    Crystal structure of hexagonal form of graphite with the stacking of ABA sequence of C atoms.

## 1.2 Diamond

Diamond is the second stable allotrope of carbon. Diamond structure is one of the most recurring crystallographic structures among covalent solids. Silicon and germanium, belonging to the fourth group, as well as the III-V and II-VI compound semiconductors such as GaAs or CdTe, also exhibit the same "diamond-like" structure. The ideal diamond structure shows each carbon surrounded by four other carbon atoms at the corners of a regular tetrahedron. The set of carbon atoms forms a very strong covalent *sp*³ hybridized σ bonds [1].
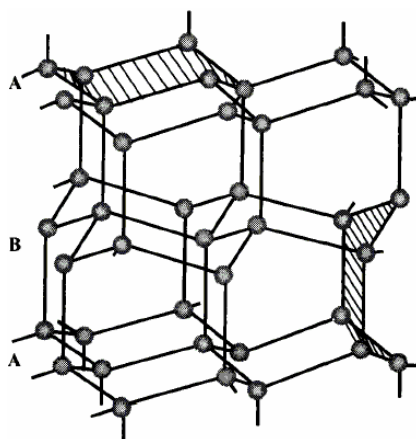


**Fig. 1.2.1**    Tetrahedrons of C atoms arranged in the diamond lattice [2].

The cubic diamond structure can be viewed as two fcc structures interpenetrated and displaced of $(¼, ¼, ¼)a_0$, where $a_0 = 3.567$ Å, is the length of the cube edge, i.e. the lattice constant. The nearest-neighbor carbon-carbon distance is 1.544 Å, which is 10% higher than that of graphite. Nonetheless it is worth to observe that the atomic density of diamond is 56% higher than in graphite, this is because of the anisotropy occurring in the graphite crystal in the c-direction which is absent in the high symmetry of the diamond structure.

Besides the two most diffused allotropes (diamond and graphite), elemental carbon has also allotropes of different and lower dimensionalities, ranging from zero-dimensional structures (0D) to the two-dimensional structures (2D). One dimensional (0D) allotropes are the fullerenes while one-dimensional structures (1D) are the carbon nanotubes. The two-dimensional (2D) allotropes are nanowalls and graphene sheets [3], respectively.

The structural properties of carbon allotropes can be easier described by the electronic configuration of the carbon atom once the orbital hybridization is considered (see Appendix A).

### 1.3 Buckminsterfullerene[1]

The discovery of carbon nanotubes in 1991 is directly connected with that of $C_{60}$ occurred in the mid eighties. $C_{60}$ is the first member of a new class of high symmetric molecules named fullerenes[1].

Fullerene ($C_{60}$) is a molecule formed by sixty carbon atoms arranged in a closed hollow cage, nearly spherical molecule. This molecule has a shape of a truncated icosahedron[2], where the sixty carbon atoms are placed at the vertices.

The $C_{60}$ molecule and the graphite have many common characteristics allowing to imagine the fullerene molecule as a "tiny-droplet" of graphene sheet. In particular in $C_{60}$ molecules (1) the nearest-neighbor carbon-carbon (C-C) distance ($a_{cc}$) is about

---

[1] In honor of Richard Buckminster Fuller (1895 - 1983), inventor, architect, engineer, mathematician, poet and cosmologist, inventor of the geodetic domes that have the same shape of half of a $C_{60}$ but quite bigger.

[2] A regular truncated icosahedron is a 32-faced Archimedean solid corresponding to an arrangement of 20 hexagons, 12 pentagons, 60 vertices and 90 edges of equal length, consistent with Euler's theorem for polyhedra:
$$f + v = e + 2$$
where f, v and e are the number of faces, vertices and edges of the polyhedron.

1.44 Å, comparable with that of graphite (1.42 Å), (2) each carbon atom both in graphite and in $C_{60}$, is bounded to three other carbon atoms with $sp^2$-like bonds and (3) the structure of fullerene is mainly constituted by hexagons. The resulting arrangement of the 60 atoms is that of a molecule having the shape of a soccer-ball [1].
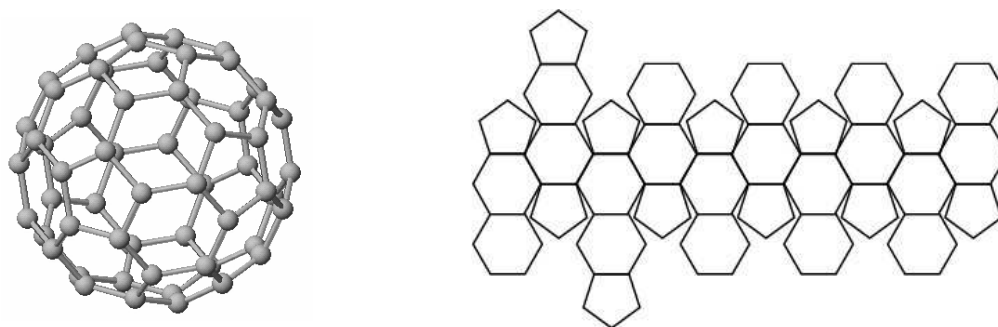


**Fig. 1.3.1**     3D view of the $C_{60}$ molecule with the evidence of carbon atoms at the vertices of the truncated icosahedron. On the right side there is a planar scheme of fullerene with the correct sequence of hexagons and pentagons.

In the proposed $C_{60}$ structure, each vertex of the truncated icosahedron is occupied by a carbon atom, and each carbon is triply bounded to other carbon atoms by one double bond and two single bonds. Two single C-C bonds connect carbon atoms at the edge of the pentagon, where hexagon and pentagon are connected. The double bond connects two carbon atoms at the edge of the hexagon, where two hexagons are joined. The lengths of these two different bonds are 1.46 Å for the single bond and 1.40 Å for the double bond.

Usually, $sp^2$ carbon and its three neighboring atoms arrange in a planar structure. The structure for $C_{60}$ is not planar with an angle between a $p_z$ axis and a C-C bond vector that is 101.6° (which is 90° in planar graphite) [4].

The curvature of the trigonal bonds in $C_{60}$ leads to an admixture of $sp^3$ bonding, characteristic of tetrahedral bonds of diamond but totally absent in graphite.

The calculated diameter for $C_{60}$ molecule is 7.09 Å, assuming that C-C distance is 1.40 Å along the edge of the hexagon and 1.46 Å along the edge of pentagon. The experimental value for fullerene diameter given by NMR measurements is $7.10 \pm 0.07$ Å [5].

## *1.4   Carbon Nanotubes*

Carbon nanotubes were discovered by Ijima in 1991 as a by-product of the arc-discharge synthesis of the $C_{60}$. Since their discovery the interest about the properties of Carbon Nanotubes (CNTs) increased very quickly [6].

Carbon Nanotubes can be considered as the tubular form of fullerenes on the dimension scale of nanometers. Transmission Electron Microscopy (TEM), Raman spectroscopy and Scanning Tunneling Microscopy (STM) confirmed that the structure of carbon nanotubes is made of all-carbon walls arranged in such a way to form concentric cylinders, with single walls having the structure of the honeycomb network of a graphene sheet.

In particular, a Single Wall Carbon Nanotube (SWNT) can be theoretically seen as a single cylinder of graphene of infinite length possibly with caps at each end that could be seen as two half-fullerenes. Those carbon nanotubes, constituted of several coaxial graphite layers, rolled up into cylinders of different diameters, are called Multi Walls Carbon Nanotubes (MWNTs). CNTs can be equally considered as single molecules because of their small dimensions (few nm in diameter and few μm in length), or as one-dimensional crystals with a translational periodicity along the tube axis. CNTs can be built in many ways varying the roll up of the graphene sheet into a cylinder. There are, in fact, a lot of diameters and possible axis orientations with respect to fixed base vectors of the graphene sheet. All these possible orientations are described by the resulting arrangement of the hexagons around the tube direction (chiral vector), in a helical pattern.

The physical properties of the SWNTs are closely connected with this arrangement. The metallic or semiconducting behavior of a SWNT depends, in fact, on its chirality.

SWNTs can be produced with different methods (i.e. Laser Ablation, Arc Discharge, and Chemical Vapor Deposition) showing quite different distributions of diameters and chiralities, tending to form bundles with a hexagonal packing during the growth process [7]. MWNTs can be grown using the CVD and AD methods showing also a large variety of diameters. The typical distance between two coaxial and adjacent layers in a MWNT is the same of two adjacent graphene layers in graphite (3.41 Å). MWNTs show lengths similar to that of SWNTs but much larger diameters.

### *1.4.1. Description of the honeycomb structure of Carbon Nanotubes*

By considering that the structure of each single cylinder forming a CNT is the same of that of a graphene sheet, it is possible to use the same crystalline lattice in order to derive the properties of a rolled-up graphene sheet.

The unit cell of graphene is individuated by the two base vectors $a_1$ and $a_2$ and contains two carbon atoms (fig. 1.4.1). The modules of the two base vectors can be easily obtained by the value of the length of *C-C* bond, once the 60° angle between the two is considered. Namely their values are: $|a_1| = |a_2| = a = \sqrt{3}a_{cc}$.

The lattice structure of a SWNT can be easily gained if we imagine cutting the wall of a tube along the axis direction after unwrapping the portion of graphene by superimposing it with an extended layer of the same material. By doing so it is possible to observe as the circumference of the unwrapped sheet corresponds to a vector on the honeycomb structure of the graphene layer. This vector results as a combination of the basis vectors and is called the chiral vector $c = n_1 a_1 + n_2 a_2$. The $c$ vector determines the fundamental structural and the physical properties of the nanotubes. The $c$ vector is called the chiral vector because it forms an angle (chiral angle) with the direction of the $a_1$ vector that determines the helical structure of the nanotube.

The chiral vector is uniquely identified by two integer numbers called the chiral indices $(n_1, n_2)$. These indices are the distinctive characteristic of each tube determining, among the physical properties, also the electronic band structure of the nanotube. The integer $n$ is the greatest common divisor of $n_1$ and $n_2$ indices, $(gcd[n_1, n_2])$, and it corresponds to the number of lattice vectors of graphene belonging to the chiral vector.

The direction of the chiral vector is measured by the chiral angle $\theta$ that, according to the definition, is calculated as follows:

$$\cos\theta = \frac{a_1 \cdot c}{|a_1| \cdot |c|} = \frac{n_1 + \frac{n_2}{2}}{\sqrt{n_1^2 + n_1 n_2 + n_2^2}}$$

Because of the particular rotational symmetry of graphene, each tube with $0° \leq \theta \leq 30°$ has another equivalent tube with $30° \leq \theta \leq 60°$, where the helix of the graphene network around the tube only changes from the right-handed to the left-handed

wrapping. Referring to the case with $n_1 \geq n_2 \geq 0$ (i.e. $30° \leq \theta \leq 60°$), it is possible to find three different types of nanotubes, classed as zig-zag, armchair and chiral. Zig-zag nanotubes are those with one of chiral indexes equal to zero i.e. $(n,0)$ while armchair nanotubes have equal chiral indexes $(n,n)$. A chiral nanotube is a nanotube that is neither armchair nor zig-zag. A picture of the three possibilities and of their characteristics is reported in table 1.1.
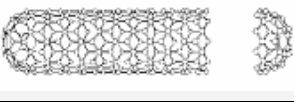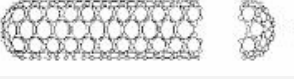
| Indices | θ | Types | Schematic | Cross section pattern |
|---------|---|-------|-----------|----------------------|
| $(n,0)$ | 0° | Zig-zag |  |  *Trans*-configuration |
| $(n,n)$ | 30° | armchair |  |  *Cis*-configuration |
| $(n_1,n_2)$ | $0 \leq |\theta| \leq 30$ | chirale |  | Mix of *cis* e *trans* |

**Table 1.1**     Classification of CNTs with the indication of chiral angle and a scheme of the edge pattern.

By wrapping a graphene sheet the nanotube is formed and the lattice points, that are the extremes of the chiral vector, will coincide. Because of the connection with the chiral vector the diameter $d$ is given by:

$$d = \frac{|\boldsymbol{c}|}{\pi} = \frac{a}{\pi}\sqrt{n_1^2 + n_1 n_2 + n_2^2} = \frac{a}{\pi}\sqrt{N} \qquad\qquad with\ N = n_1^2 + n_1 n_2 + n_2^2$$

Along with the chiral vector, in order to define an elementary cell for a nanotube, it is introduced another vector, the translation vector. The translational vector $\boldsymbol{T}$ is the shortest lattice vector perpendicular to the chiral vector $\boldsymbol{c}$. Together these two vectors individuate the elementary cell of the nanotube. By imposing the perpendicularity condition between $\boldsymbol{T}$ and $\boldsymbol{c}$ vectors we find:

$$\boldsymbol{T} \equiv (t_1, t_2) \qquad \boldsymbol{T} = t_1\boldsymbol{a_1} + t_2\boldsymbol{a_2} \qquad \boldsymbol{T} = -\frac{2n_2 + n_1}{nR}\boldsymbol{a_1} + \frac{2n_1 + n_2}{nR}\boldsymbol{a_2}$$

$$T = |\boldsymbol{T}| = \frac{\sqrt{3\left(n_1^2 + n_1 n_2 + n_2^2\right)}}{nR}a \qquad R = \begin{cases} 3 & \dfrac{n_1 - n_2}{3n} \in N \\ \\ 1 & otherwise \end{cases}$$

where $R$ is an integer value that can be only 1 or 3 depending on the values of $n_1$ and $n_2$. Some examples of the chiral vectors $c$ for zig-zag, armchair and chiral CNTs are shown in fig. 1.4.1.
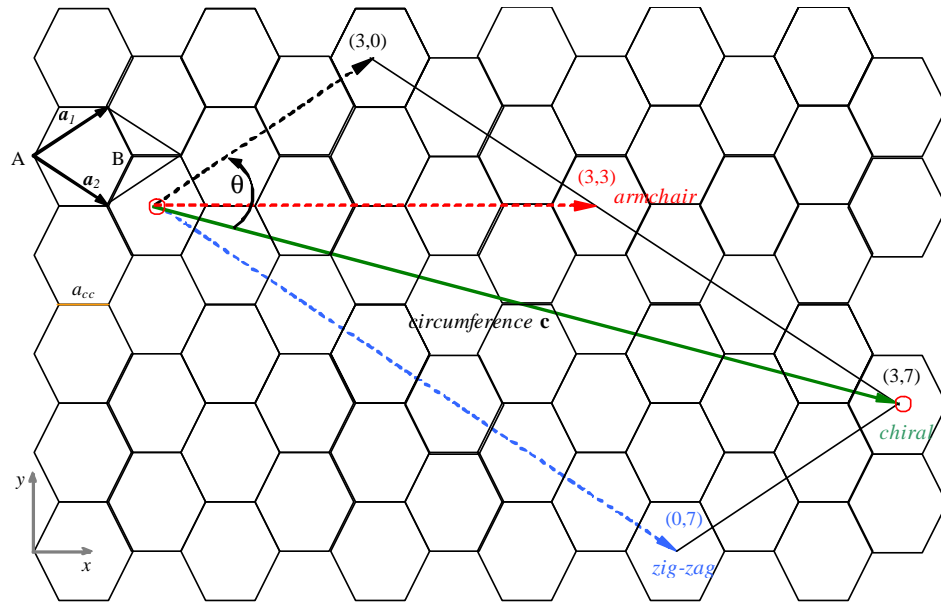


**Fig. 1.4.1**    Graphene honeycomb lattice and lattice vectors $\boldsymbol{a_1}$ and $\boldsymbol{a_2}$. Some examples of CNTs (zig-zag in blue, armchair in red and chiral in green).

Let's consider now the unitary cell determined by a nanotube. The unitary cell of a nanotube is the portion of cylindrical surface having a height (parallel to the axis) equal to the length of the translational vector, and the diameter as determined by the wrapping of the chiral vector. Referring to the definition, the unitary cells will contain many or few carbon atoms depending on the chiral indices [8],[9] (fig. 1.4.2).
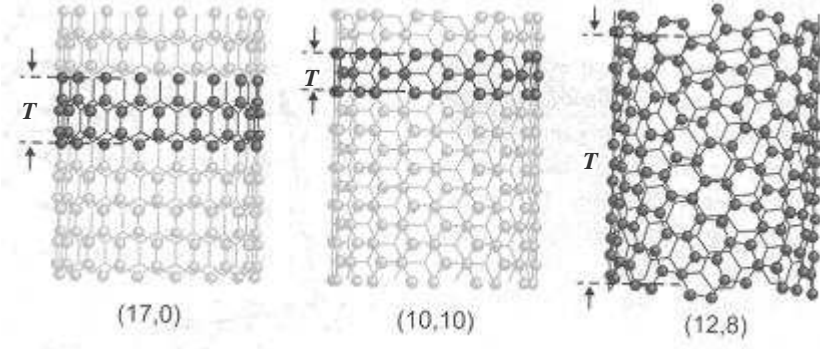
**Fig. 1.4.2**    In dark are shown the unit cells of the (17,0), (10,10) and (12,8) nanotubes respectively [10].

The number of carbon atoms $n_c$, contained in the unit cell is obtained from the ratio between the area $S_t$ of the cylinder and the area $S_g$ of the hexagonal unit cell of graphene. The ratio between these two values gives the number $q$ of graphene hexagons in the unit cell. The hexagonal cell of graphene contains two carbon atoms because each carbon atom at each vertex is shared with other three hexagons, therefore the total number of C-atoms in the CNT unit cell is:

$$n_c = 2q = 2\frac{S_t}{S_g} = \frac{4\left(n_1^2 + n_1 n_2 + n_2^2\right)}{nR}$$

The expressions of the lattice parameters **c** and **T** for achiral tubes like zig-zag and armchair are resumed in table 1.2.

| Type | Indices | $N$ | $n_c$ | $R$ | $d$ | $|T|$ | $\theta$ |
|------|---------|-----|-------|-----|-----|-------|----------|
| $\mathcal{A}$ | $(n,n)$ | $3n^2$ | $4n$ | $3$ | $\dfrac{\sqrt{3}na}{\pi}$ | $A$ | $30°$ |
| $\mathcal{Z}$ | $(n,0)$ | $n^2$ | $4n$ | $1$ | $\dfrac{na}{\pi}$ | $\sqrt{3}a$ | $0°$ |
| $\mathcal{C}$ | $(n_1,n_2)$ | $n_1^2 + n_1 n_2 + n_2^2$ | $\dfrac{4N}{nR}$ | $-$ | $\dfrac{\sqrt{N}a}{\pi}$ | $\dfrac{\sqrt{3N}a}{nR}$ | $\arccos \dfrac{n_1 + \dfrac{n_2}{2}}{\sqrt{N}}$ |

**Table 1.2**    Principal parameters of armchair ($\mathcal{A}$), zig-zag (Z) and chiral (C) nanotubes.

### *1.4.2 Direct and reciprocal lattice of a graphene sheet*

The primitive cell (i.e. the Wigner-Seitz cell) of the reciprocal lattice is known as the first Brillouin zone. This cell can be determined by tracing from a lattice point all the lines directed to the first neighbors, and cutting each line in the middle with an orthogonal plane. By doing so we will obtain a polyhedron, the Wigner-Seitz cell, containing the original lattice point [11].

In the case of a hexagonal lattice the reciprocal lattice is a hexagonal lattice too, where the base vectors are $b_1$ and $b_2$.
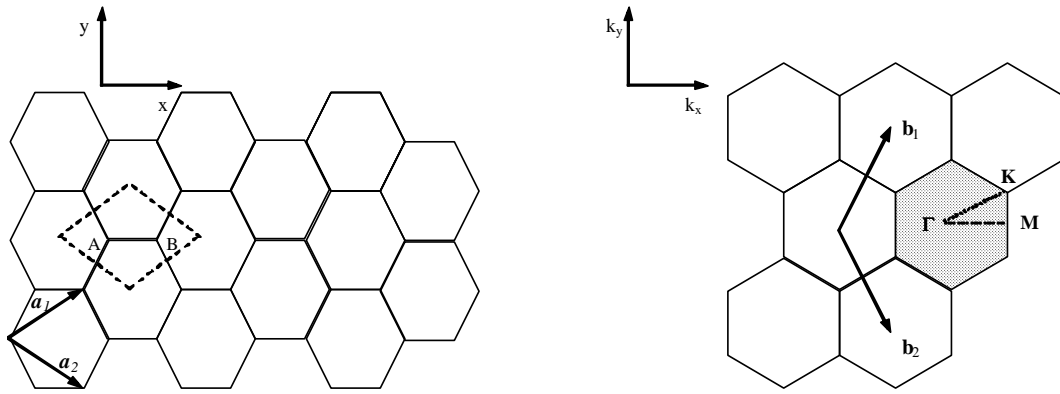


**Fig. 1.4.3**    On the left the direct lattice of graphene with the unit cell indicated with dashed lines. On the right the reciprocal lattice with base vectors $b_1$ and $b_2$ where the shaded area is the first Brillouin zone.

The coordinates of reciprocal lattice vectors are connected to that of the direct lattice from the relations of ortho-normality. In the coordination system of $k_x$ and $k_y$, showed in figure 1.4.3, the reciprocal lattice vectors, corresponding to the unit vectors $a_1$, $a_2$ and $a_3$ of the direct lattice, have hence the coordinates:

$$b_1 = 2\pi \frac{a_2 \times a_3}{a_1 \cdot (a_2 \times a_3)} \qquad b_2 = 2\pi \frac{a_3 \times a_1}{a_1 \cdot (a_2 \times a_3)} \qquad b_3 = 2\pi \frac{a_1 \times a_2}{a_1 \cdot (a_2 \times a_3)} \qquad a_3 = T \hat{z}$$

$$b_1 \equiv \left( \frac{2\pi}{\sqrt{3}a}, \frac{2\pi}{a}, 0 \right) \qquad b_2 \equiv \left( \frac{2\pi}{\sqrt{3}a}, -\frac{2\pi}{a}, 0 \right) \qquad b_3 \equiv \left( 0, 0, \frac{2\pi}{T} \right)$$

$$|b_1| = |b_2| = b = \frac{4\pi}{\sqrt{3}a} \qquad\qquad\qquad |b_3| = \frac{2\pi}{|T|}$$

The modules of $b_1$ and $b_2$ determine the lattice parameters of the reciprocal space. All main parameters for carbon nanotubes are resumed in table 1.3.

| Symbol | Name | Formula | Value |
|:---:|:---:|:---:|:---:|
| $a$ | Length of unit vector | $a = \sqrt{3}a_{cc}$ | $a = 2.49$ Å<br>$a_{cc} = 1.44$ Å |
| $\boldsymbol{a_1, a_2}$ | Unit vectors | $\left(\dfrac{\sqrt{3}}{2}a, \dfrac{a}{2}\right), \left(\dfrac{\sqrt{3}}{2}a, -\dfrac{a}{2}\right)$ | — |
| $\boldsymbol{b_1, b_2}$ | Reciprocal lattice vectors | $\left(\dfrac{2\pi}{\sqrt{3}a}, \dfrac{2\pi}{a}\right)$<br><br>$\left(\dfrac{2\pi}{\sqrt{3}a}, -\dfrac{2\pi}{a}\right)$ | — |
| $\boldsymbol{c}$ | Chiral vector | $\boldsymbol{c} = n_1\boldsymbol{a_1} + n_2\boldsymbol{a_2} \equiv (n_1, n_2)$ | — |
| $c$ | Length of chiral vector | $c = \left\| \boldsymbol{c} \right\| = a\sqrt{n_1^2 + n_1 n_2 + n_2^2}$ | — |
| $d$ | Diameter | $d = \dfrac{\|\boldsymbol{c}\|}{\pi} = \dfrac{a}{\pi}\sqrt{n_1^2 + n_1 n_2 + n_2^2}$ | — |
| $\theta$ | Chiral angle | $\cos\theta = \dfrac{n_1 + \dfrac{n_2}{2}}{\sqrt{n_1^2 + n_1 n_2 + n_2^2}}$<br><br>$\sin\theta = \dfrac{\sqrt{3}n_2}{\sqrt{n_1^2 + n_1 n_2 + n_2^2}}$ | $0 \le \|\theta\| \le \dfrac{\pi}{6}$ |
| $R$ | gcd $(n_1 - n_2, 3n)$ | $R = \begin{cases} 3 & \dfrac{n_1 - n_2}{3n} \in \mathbb{N} \\ \\ 1 & otherwise \end{cases}$ | — |
| $\boldsymbol{T}$ | Translational vector | $\boldsymbol{T} = t_1\boldsymbol{a_1} + t_2\boldsymbol{a_2} \equiv (t_1, t_2)$ | — |
| $q$ | Number of hexagons in the nanotube unit cell | $q = \dfrac{2\left(n_1^2 + n_1 n_2 + n_2^2\right)}{nR}$ | — |

**Table 1.3**     Main parameters of carbon nanotubes.

### *1.4.3 Unit cell and Brillouin zone of a Carbon Nanotube: zone-folding approximation*

The unit cell of a carbon nanotube in the real space is the rectangular portion of the graphene sheet built with the chiral vector *c* and translational vector *T* as shown in figure 1.4.4.
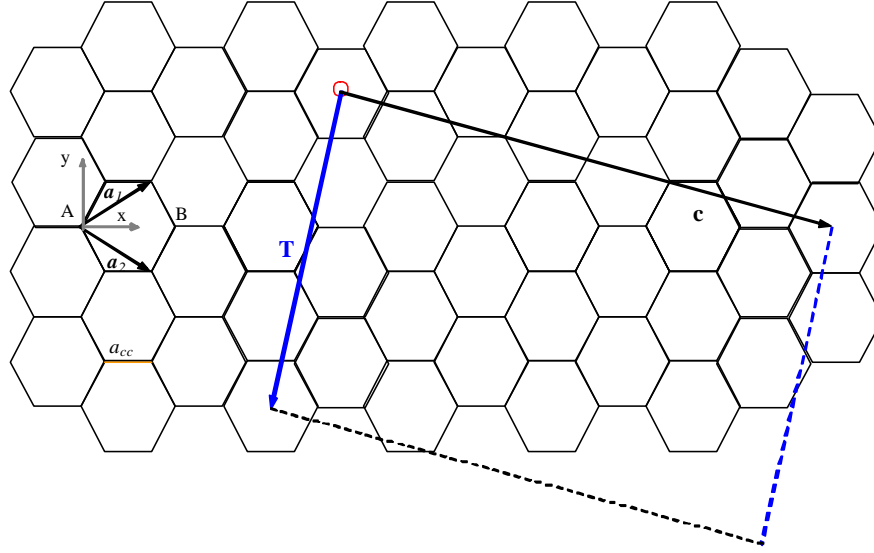


**Fig. 1.4.4**      Hexagonal lattice of graphene with the evidence of chiral vector *c*, translational vector *T* and unit cell of the nanotube in the real space.

The Brillouin zone of a nanotube can be built by using the $k_z$ and $k_\perp$ vectors that correspond to the *T* and *c* vectors in the reciprocal space. $k_z$ is the reciprocal lattice vector corresponding to the translational period *T* along the nanotube *z* axis and its length is $\frac{2\pi}{T}$. By considering the nanotube like a one-dimensional system of infinite length, the translational symmetry of the *T* vector imposes to the wave vectors in the $k_z$ direction to be continuous. Differently for a carbon nanotube of finite length *L*, the spacing between two consecutive wave vectors is $\frac{2\pi}{L}$.

The vector of the reciprocal lattice corresponding to the *c* vector along the circumference of the nanotube is $k_\perp$. The boundary conditions arising from the cylindrical structure of the nanotube lead to the quantization of $k_\perp$ that can assume only discrete values. The expressions of the reciprocal lattice vectors $k_z$ and $k_\perp$, respectively

along the tube axis and along the circumference, are obtained from that of the real space vectors $R_i$, starting from the relations $R_i \cdot k_j = 2\pi\delta_{ij}$.

$$R_1 = c \qquad \Rightarrow \qquad c \cdot k_1 = 2\pi \qquad c \cdot k_2 = 0$$
$$R_2 = T \qquad \Rightarrow \qquad T \cdot k_2 = 2\pi \qquad T \cdot k_1 = 0$$
$$k_1 = k_\perp \qquad\qquad\qquad k_2 = k_z \qquad\qquad\qquad (e_{I.1})$$

It is possible to write $k_z$ and $k_\perp$ in a general form as a combination of $b_1$ and $b_2$. Therefore the expressions for $k_z$ and $k_\perp$ become:

$$k_\perp = \frac{1}{q}\left(-t_2 b_1 + t_1 b_2\right) \qquad\qquad k_z = \frac{1}{q}\left(n_2 b_1 - n_1 b_2\right) \qquad\qquad (e_{I.2})$$

The first Brillouin zone of a one-dimensional material is a segment. Therefore for a carbon nanotube the first Brillouin zone is the segment of length $\frac{2\pi}{T}$, i.e., the modulus of $k_z$. Since $t_1$ and $t_2$ don't have any common divisor, except the unity, any of the $q - 1$ vectors $\mu k_\perp$ (where $\mu = 1,..., q - 1$), reported in the $(e_{I.2})$, is a reciprocal lattice vector of the two-dimensional graphite. Hence the $q$ wave vectors $\mu k_\perp$ ($\mu = 1,..., q - 1$) originate $q$ discrete vectors $k$. These vectors individuate $q$ parallel segments representing the Brillouin zone of a nanotube (the $q$ lines are parallel to the $k_z$ vectors; their length is $\frac{2\pi}{T}$ while their separation is $\frac{2\pi}{L}$). The $k$ vectors assume all values in the range ($-\frac{\pi}{T}$, $\frac{\pi}{T}$).

### 1.4.4 Zone-folding Approximation

Carbon nanotube bands consist of a group of one-dimensional energy dispersion relations arising from the dispersion relations of two-dimensional graphite (*zone folding* approximation) by cutting along $q$ lines parallel to the nanotube axis direction (i.e. along the allowed $k$ values indicated in the Paragraph 1.4.3).

The valence and semiconducting bands of graphene cross each other at the **K** point of the Brillouin zone (see Appendix C). Therefore if this point is included among the allowed states of a carbon nanotube, then the nanotube is metallic otherwise it is semiconducting.

The electronic states of a carbon nanotube are restricted to such $k$ vectors fulfilling the condition $c \cdot k = 2\pi m$ (with $m \in$ N). If the **K** point satisfies this condition for the considered nanotube, the CNT will be metallic, otherwise it will be semiconducting. In terms of reciprocal lattice vectors (see figure 1.4.3), the **K** point could be written as in ($e_{I.3}$). The **K** point belongs to the nanotube Brillouin zone if the second expression in the ($e_{I.3}$) is fulfilled:

$$K = \frac{1}{3}(2b_2 - b_1)$$

$$c \cdot K = (n_1 a_1 + n_2 a_2) \cdot \frac{1}{3}(2b_2 - b_1) = 2\pi m \qquad (e_{I.3})$$
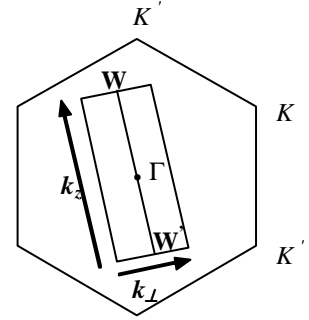


**Fig. 1.4.5**   WW$^{'}$ is the first Brillouin zone of a nanotube. $K$ points and $k_z$ e $k_\perp$ vectors are indicated in figure.

Developing the ($e_{I.3}$) by using the expressions of $a_1$, $a_2$, $b_1$ and $b_2$ and developing the scalar products, the conditions on the $n_1$ and $n_2$ indices are obtained, that distinguish between metallic and semiconducting nanotubes:

$$\begin{cases} \dfrac{n_1 - n_2}{3} \neq m \quad \Rightarrow \quad semiconducting \quad nanotube \\[2mm] \dfrac{n_1 - n_2}{3} = m \quad \Rightarrow \quad metallic \quad nanotube \end{cases} \qquad m \in \text{N} \qquad (e_{I.4})$$

This means that only the ($n_1$,$n_2$) nanotubes, whose difference $n_1$-$n_2$ is a multiple of 3, are metallic otherwise they are semiconducting [12],[13]. This condition for $n_1$ and

$n_2$ indices is equivalent to the condition $\dfrac{2n_1 + n_2}{3} = m$ because this is fulfilled if the relations ($e_{I.4}$) are fulfilled. The *zone folding* approximation allows distinguishing between the metallic and semiconducting nature of carbon nanotubes. Only $\left(\dfrac{1}{3}\right)$ of nanotubes is metallic while the remaining $\left(\dfrac{2}{3}\right)$ is semiconducting.
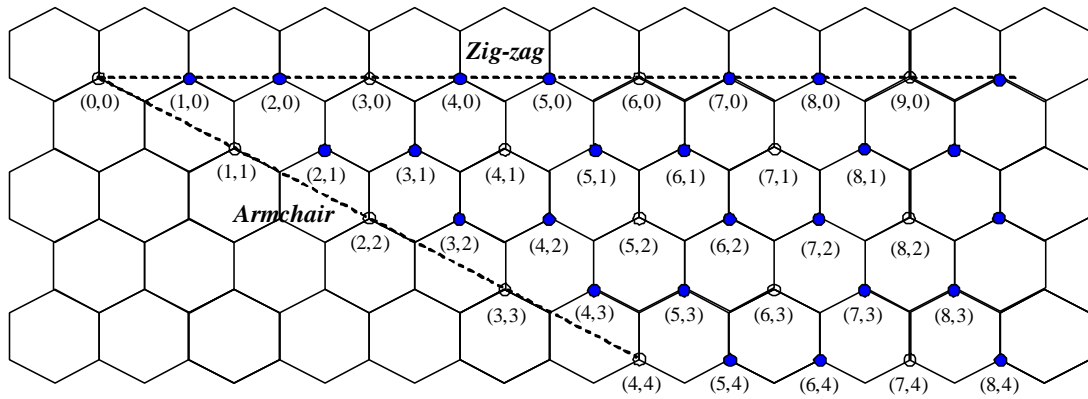


**Fig. 1.4.6**     The metallic and semiconducting CNTs indicated respectively with open and blue solid circles on the map of chiral vectors ($n_1,n_2$).

In particular the *armchair* nanotubes having the same indices (*n,n*), are always metallic while the *zig-zag* tubes with indices (*n*,0) are metallic only if *n* is a multiple of 3. All the metallic and semiconducting nanotubes ($n_1,n_2$) are showed in figure 1.4.6, depicted on a graphene plane.

## 1.5  *Energy dispersion relations of Carbon Nanotubes*

In order to determine the electronic band structure of a carbon nanotube, because of the wrapped structure that can be derived from that of a graphene layer, we have to consider how the electrons behave in a graphene sheet. As already seen, every C-atom in the hexagonal structure involves three orbitals *s*, $2p_x$ and $2p_y$ that are hybridized in a $sp^2$ configuration producing three $\sigma$ bonds in the plane. Whereas the $2p_z$ orbital, that is perpendicular to the graphite plane, produces the $\pi$ covalent bonds. The covalent $\pi$ bonds give the most important contribute to the electronic properties of graphene.

When a graphene plane is rolled up to form a nanotube, the σ bonds form, along the nanotube wall, a hexagonal network that is the same found in the pure graphite with the addition of a slight bending effect. The π bonds are instead responsible also for weak van der Waals interactions between different tubes and they determine the band structure.

### 1.5.1 Energy dispersion relations of 2D-graphite and π bands

Theoretical calculations arising from first principles method, have demonstrated that the gap between bonding and antibonding σ and σ* bands, is about 11 eV [14], [15]. As a consequence, in a first approximation these two bands don't contribute to the electronic properties of the graphene being their energy difference so high.

For what concerns the π band a tight binding model can be used to obtain the energy level of the π valence and conduction bands of a graphene, successively extending these results in order to determine the band structure of the carbon nanotube (Appendixes B and C). We start from the Schrödinger equation of the system of C-atoms in the graphene lattice and we introduce the Block functions as linear combination of the atomic wave functions. After that we solve the Schrödinger equation in the first neighbors' approximation, considering negligible the overlapping between wave functions centered on different atoms. All the tight binding calculations developed to obtain the final expressions ($e_{B.16}$ and $e_{B.17}$) of the energy dispersion relations have been extensively reported in the Appendix B.

The most general expression of the energy bands of graphene, without neglecting the overlapping integral between nearest neighbors atoms and considering the value of $\varepsilon_{2p}$ constant, is:

$$\begin{cases} \varepsilon_{2p} = 0 \\ E^{\pm} = = \dfrac{\pm \gamma_0 \sqrt{f}}{1 \pm s_0 \sqrt{f}} \end{cases}$$

(*$e_{B.17}$* of Appendix B)

$$f(\boldsymbol{k}) \quad = 4\cos\left(\frac{\sqrt{3}}{2}ak_x\right)\cos\left(\frac{a}{2}k_y\right) + 4\cos^2\left(\frac{a}{2}k_y\right) + 1$$

$\varepsilon_{2p}$ is the term accounting for the self interaction (the interaction of the C atom with itself), and it represents the energy of the orbital $2p_z$. $\gamma_0$ is the C – C interaction term that gives a measure of the interaction energy between two nearest neighbor atoms and $s_0$ is the overlap integral between the wave functions of two nearest neighbor carbon atoms.

The value of $\gamma_0$ is negative while $s_0$ is positive. These values come from the first principles calculations of the graphite energy bands. Therefore, the valence and conduction bands of two-dimensional graphite are (for the details refer to the Appendix B):

$$\begin{cases} E^+ = \dfrac{\gamma_0\sqrt{f}}{1+s_0\sqrt{f}} & \text{\textit{Valence band }} \pi \\[4mm] E^- = \dfrac{-\gamma_0\sqrt{f}}{1-s_0\sqrt{f}} & \text{\textit{Conduction band }} \pi^* \end{cases} \qquad (e_{B.18}\text{ of Appendix B})$$

The energy dispersion relations for the graphene in the nearest neighbors' approximation ($s_0 = 0$) are:

$$E_{S=0}^{fn\ \pm}(k) = \pm|H_{AB}(k)| = \pm\gamma_0\left[1 + 4\cos\left(\frac{\sqrt{3}}{2}ak_x\right)\cos\left(\frac{a}{2}k_y\right) + 4\cos^2\left(\frac{k_ya}{2}\right)\right]^{\frac{1}{2}}$$

$$(e_{B.16}\text{ of Appendix B})$$

The energy dispersion relations of the 2D graphite, plotted throughout the whole Brillouin zone, are reported in the Appendix C. These plots have been obtained by using a specific software program implemented with MatLab. At first approximation, the carbon nanotubes properties are connected to the properties of the two-dimensional graphite when, from the band structure of graphene, the lines corresponding to the nanotube Brillouin zone are selected. Therefore the band structure of a particular carbon nanotube is found by cutting the two-dimensional graphene bands along suitable directions.

### *1.5.2 Energy dispersion relations of Armchair and Zig-zag Nanotubes*

To obtain the energy dispersion relations of armchair and zig-zag nanotubes starting from the energy dispersion relations of two-dimensional graphite ($e_{B.16}$ of Appendix B), it is necessary to use the appropriate boundary conditions that determine the allowed $k$ wave vectors.

The cuts that determine the set of bands for a CNT are made along the $\mu k_\perp$ direction. The number of bands is exactly the double of the number of quantized $k_\perp$ vectors arising from the periodic boundary conditions on $c$, i.e. $2q$ ($q$ is number of hexagons in the unit cell). The range of variation of $k$ values for the energy dispersion relations of a nanotube is defined from the length of $k_z$ vector.

For ($n,n$) armchair CNTs the periodic boundary conditions define a suitable number of allowed $k_\perp$ vectors along the circumferential direction. A representation of a part of the unit cell and the Brillouin zone for an armchair nanotube is reported in figure 1.5.1. In this figure $k_z$ corresponds to the $T$ vector of the unit cell and it is obtained using the ($e_{I.2}$).
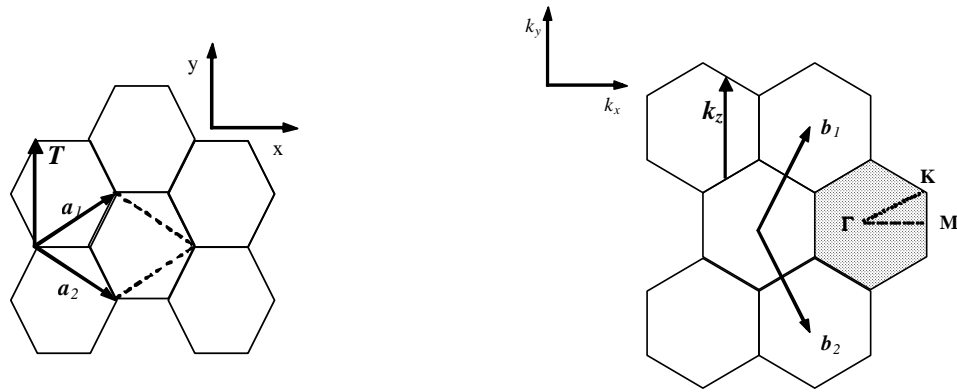


**Fig. 1.5.1**    On the left part a little portion of the unit cell of an armchair tube with unit vectors $a_i$. On the right part the extended Brillouin zone of an armchair tube where $k_z$ corresponds to $T$ ($k_z = \frac{1}{2}(b_1 - b_2)$ ; $T = a_1 - a_2$).

For an armchair tube the $\mathbf{k}_\perp$ vector has only $k_{\perp x}$ component and the range of variation of $k_y$ coincides with the modulus of $\mathbf{k}_z$ vector, therefore using the $(e_{I.1})$ and $(e_{I.2})$ we obtain:

$$\mathbf{c} \cdot \mathbf{K} = 2\pi m \qquad\qquad n\sqrt{3}a \cdot k_{\perp mx} = 2\pi m \qquad\qquad \begin{array}{c} m = 1, \dots, q \\[6pt] q = 2n \end{array}$$

$$k_{zx} = 0 \qquad\qquad \left| k_{zy} \right| = \frac{\left| \mathbf{b_1} - \mathbf{b_2} \right|}{2} = \frac{2\pi}{a} \qquad\qquad armchair$$

The ($e_{B.16}$ of Appendix B) for an armchair nanotube becomes ($e_{I.5}$):

$$E_m^a(\mathbf{k}) = \pm\gamma_0 \left[ 1 + 4\cos\left(\frac{\pi m}{n}\right)\cos\left(\frac{a}{2}k_y\right) + 4\cos^2\left(\frac{k_y a}{2}\right) \right]^{\frac{1}{2}} \qquad (e_{I.5})$$

$$-\pi < k_y a < \pi \qquad\qquad m = 1, \dots, 2n$$

For example the total number of bands of a (5,5) armchair nanotube is $4n = 20$. Six dispersion relations correspond to the conducting bands and other six correspond to valence bands. Two of these six are nondegenerate while the remaining four are doubly degenerate. This behavior is the same for conducting and valence bands.

For $(n,0)$ zig-zag CNTs the same considerations made for the armchair tubes could be done, by imposing periodic boundary conditions that define the suitable allowed $\mathbf{k}_\perp$ vectors. This allows deriving energy dispersion relations for a zig-zag nanotube. Repeating the same calculations done before with the help of figure 1.5.2 and of the ($e_{I.2}$), we obtain that $\mathbf{k}_z = -\dfrac{\mathbf{b_2}}{2}; \mathbf{T} = \mathbf{a_1} - 2\mathbf{a_2}$.
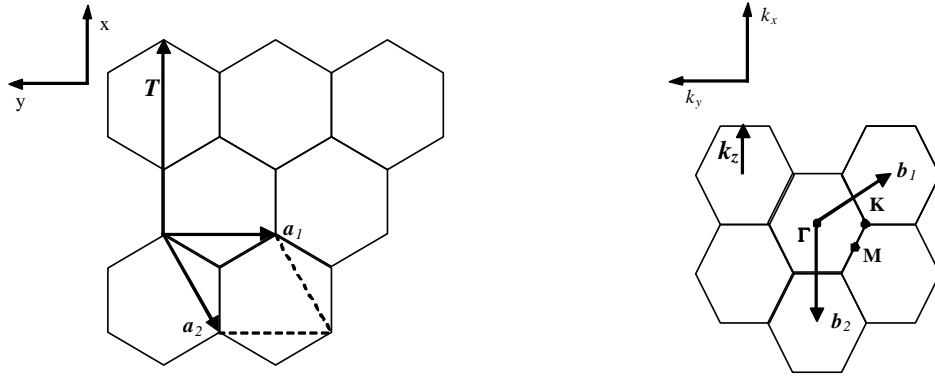
**Fig. 1.5.2**    On the left part a little portion of the unit cell of a zig-zag tube with unit vectors $a_i$ and the corresponding $T$ vector. On the right part the extended Brillouin zone of a zig-zag tube where $k_z$ is related to $T$ ($k_z = -\dfrac{b_2}{2}$; $T = a_1 - 2a_2$).

For a zig-zag tube the $k_\perp$ vector has only $k_{\perp y}$ component and the range of variation of $k_x$ coincides with the modulus of the $k_z$ vector, therefore using the ($e_{I.1}$) and ($e_{I.2}$) we obtain:

$$c \cdot K = 2\pi m \qquad\qquad na \cdot k_{\perp my} = 2\pi m \qquad\qquad \begin{aligned} m &= 1, \dots, q \\ q &= 2n \end{aligned}$$

$$\left| k_{zx} \right| = \frac{\left| b_2 \right|}{2} = \frac{2\pi}{\sqrt{3}a} \qquad\qquad k_{zy} = 0 \qquad\qquad \textit{Zig-Zag}$$

The ($e_{B.16}$ of Appendix B) for an armchair nanotube becomes ($e_{I.6}$):

$$E_m^z(\boldsymbol{k}) = \pm\gamma_0 \left[ 1 + 4\cos\left( \frac{\sqrt{3}}{2} a k_x \right) \cos\left( \frac{\pi m}{n} \right) + 4\cos^2\left( \frac{\pi m}{n} \right) \right]^{\frac{1}{2}} \qquad (e_{I.6})$$

$$-\frac{\pi}{\sqrt{3}} < k_x a < \frac{\pi}{\sqrt{3}} \qquad\qquad m = 1, \dots, 2n$$

In the general case of $(n,0)$ zig-zag nanotubes, it is possible to observe a zero energy gap at $k = 0$ for values of $n$ multiple of 3 and an energy gap when $n$ is not a multiple of 3. In the Appendix C are reported the results of a MatLab Program

implemented ad hoc to plot the zig-zag and armchair energy dispersion relations in the particular cases of a (3,3) armchair, (3,0) metallic and (4,0) semiconducting zig-zag nanotubes. The energy dispersion relations of these three kinds of nanotubes are plotted in the Appendix C.

## 1.6    *Synthesis of Carbon Nanotubes*

The great interest about the properties of carbon nanotubes (CNTs) has led to a progressive improvement of CNTs growth methods in the last fifteen years. CNTs can nowadays be synthesized by using different methods such as the arc discharge (AC), the laser ablation (LA), the catalytic chemical vapor deposition CCVD. The main factor driving the interest towards the use of one method of growth with respect to another is connected with the possible applications of the carbon nanotubes. As a general fact, for example, arc discharge methods are preferred in order to obtain an un-supported growth of bulk materials. On the other hand, because of their remarkable electronic properties, the interest in the CNTs synthesis is mainly devoted towards those techniques allowing to gain a control on the localization of carbon nanotubes as well as on the type and chirality. Among the different methods developed until now, the catalytic chemical vapor deposition method meets the requirement of the ultra large scale integration (ULSI) process exploited in the microelectronic industry. Moreover, the CCVD methods can be also used in order to obtain a bulk production of CNTs.

### 1.6.1 Arc Discharge

Carbon Nanotubes were observed and recognized for the first time by Iijima in the carbon deposit of the arc discharge equipment used for the synthesis of fullerenes [6]. The arc discharge technique consists in the evaporation of two graphite rods, about $5 \div 20$ mm in diameter and separated by ~ 1 mm gap, by the application of a high dc voltage in an inert gas atmosphere (Ar or He) [16].

The inert gas is introduced after the evacuation of the system by a vacuum pump to reach the arc condition at about 500 torr of He or Ar. The voltage across the electrodes can vary in the range of 20 – 25 V with a dc electric current flowing between the electrodes in the range of 50 – 120 A. A schematic of the deposition apparatus and the soot formation is shown in fig. 1.6.1.

**a)**

**b)**
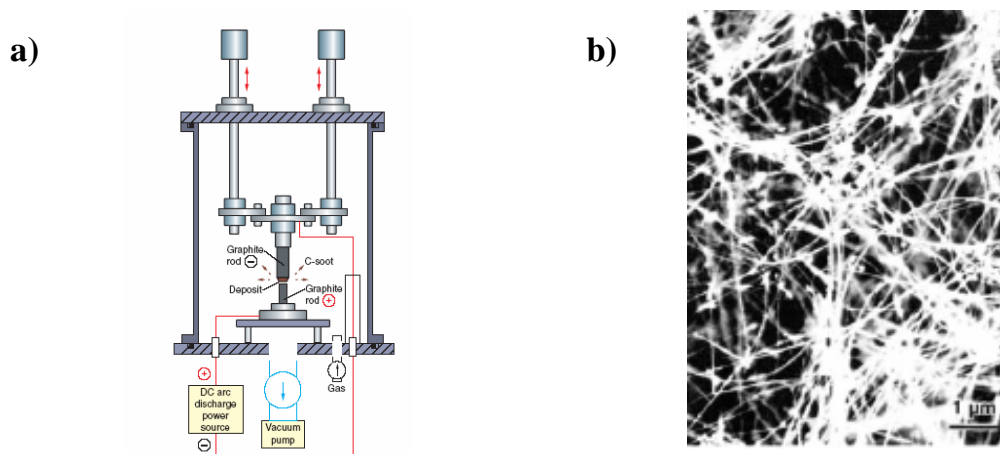


**Fig. 1.6.1** **a)** Cross-sectional view of a schematic of an arc discharge apparatus. **b)** Carbon soot containing MWNTs after an arc discharge process [16].

The evaporation of the anode forms soot onto the walls of the reactor, whereas a small part of the evaporated anode is deposited on the cathode. Carbon nanotubes were found for the first time in these deposits in the inner region of the cathode where the temperature is at the maximum (2500 – 3000 °C).

The Arc Discharge allows the large scale synthesis of nanotubes. The first tubes to be discovered with this technique were MWNTs. Using graphite rods containing metal catalysts (Fe, Co, etc.) [17],[18] as anode and pure graphite as cathode, SWNTs could form a web-like structure in the soot present in the gas phase and not as a cathode deposit [19]. Kataura and coworkers [17] found that SWNTs of different diameters and band gaps (fig. 1.6.2) can be grown, starting from arc discharge, using carbon cathodes doped with small amounts of transition metals as NiY (4.2 ÷ 1 %), NiCo (1.2 %), Ni (0.6 %) and RhPd (1.2 %)).
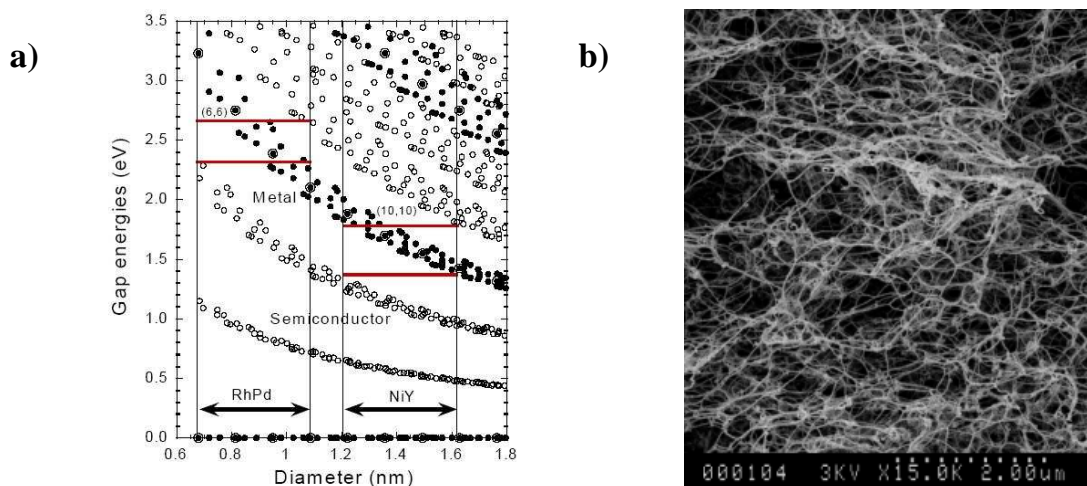
**Fig. 1.6.2**    **a)** Calculated gap energies as function of diameters for SWNTs synthesized with different catalysts. The arrows show diameter distributions for each catalyst [17]. **b)** As-prepared arc-synthesized SWNTs.

The growth of MWNTs produced in this way can be controlled through the process parameters such as the pressure of inert gas and the arcing current. The degree of crystalline quality and the yield of CNTs produced in this way were increased for the first time at gram level by using the purification processes implemented by Ebbesen and Ajayan [20]. A problem in this method is the difficulty to produce well aligned CNTs.

### 1.6.2 Laser Vaporization

The synthesis of CNTs by laser ablation has been developed in the past years starting from the first results reported by R. Smalley group [21],[22]. Laser ablation of carbon nanotubes consists in a development of the technique used for the synthesis of the fullerene $C_{60}$, where a set of very energetic excimer lasers focus their beam on a graphite target containing a portion of the transition metal needed as a catalyst. The advancement of the synthesis methods in the case of carbon nanotubes followed an inverse route to that of fullerenes. They were, in fact, first discovered in the arc discharge cathode residue. Subsequently, Smalley and co-workers set up a laser vaporization process more powerful than that used in order to obtain the $C_{60}$. This method produces bundles of SWNTs with a narrow diameter size distribution and with a very high yield conversion of graphite into nanotubes (70 % ÷ 90 %).

Schematically the method involves the vaporization of a graphite target by using powerful lasers (usually YAG or $CO_2$) [23]. The carbon target is ablated by the lasers and vaporized in an Ar atmosphere used as a buffer and carrier gas. Hence the vaporized molecules are collected on a cool plate, where they can form nanotubes and fullerenes or amorphous deposits (Fig. 1.6.3).
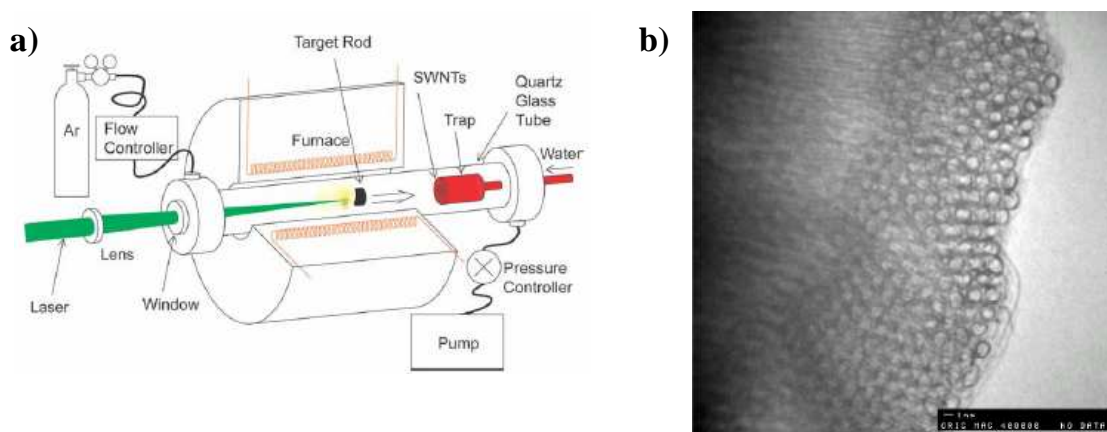


**Fig. 1.6.3**     **a)** Schematic of a laser-furnace apparatus. **b)** Hexagonal packed ropes of SWNTs [16].

If a pure graphite target is used, MWNTs are produced but if the target is doped with a low percentage of catalysts, added to graphite, SWNT growth can be observed. SWNT diameters can be controlled by modifying the laser flow and rates as well as metal catalysts. The produced high quality SWNTs have strongly peaked diameters, ranging between 10 and 20 nm, and, due to the van der Waals interaction, they result organized in ropes packed into hexagonal crystals. They reach lengths up to 100 μm or more.

An optimization of the growth can be obtained as suggested by Journet and his coworkers, adding a small percentage of yttrium and nickel as catalyst in the carbon anode [24].

### 1.6.3 Catalytic Chemical Vapor Deposition

Differently from the fullerenes, the carbon nanotubes can be synthesized by means of a catalytic decomposition process named catalytic chemical vapor deposition

(CCVD). The CCVD is a chemical method for the production of carbon nanotubes, based on the thermal decomposition of hydrocarbons in the presence of metal catalysts.

The CCVD technique is a more versatile technique with respect to the other two processes listed above. There are, in fact, a series of advantages using a catalytic CVD for the growth of carbon nanotubes. First of all, the CCVD synthesis is usually a supported growth, meaning that the synthesis can be performed on substrates with the possibility to extend the deposition process on a large scale as required by the industrial ultra large scale integration processes (ULSI). The main factors controlling a CCVD synthesis are the catalysts (form and state), the nature of the substrate and its interaction with the catalyst, the physical parameters such as temperature and pressure of the process and the species used as carbon feedstock (hydrocarbons, alcohols, complex organic derivatives).

CCVD apparatus can be easily modified into a PECVD (plasma enhanced chemical vapor deposition) apparatus, a MWCVD (micro wave CVD), a MHCVD (microwave heating CVD), a CVD apparatus equipped with polarizing electrodes. Lastly a CCVD is also easier to obtain since in its minimal configuration only a tube furnace is needed and lower temperature are required with respect to the case of the arc discharge and laser ablation method. As a matter of fact the research on the synthesis and growth of CTNs is focused on the CCVD technique in order to further improve the performances of the catalyst and hence allowing a further lowering of the process temperature. Very recent papers report SWNTs and MWNTs produced by laser ablation at room temperature simply adding $In_2O_3$, $PbO_2$ and In to pure Co-Ni target [25].

The chemical vapor deposition allows the matching of certain requirements of microelectronic industry. In fact, the use of carbon nanotubes as active (CNT-FETs) and passive elements (interconnects, vias, diodes) in the future nanoelectronic industry is closely connected with the possibility of inserting the synthesis or the processing of such material within large scale integration process of nowadays microelectronic industry. For this reason the CCVD technique results to be the most appropriate to develop this approach. In the CCVD, the possibility to employ lower substrate temperatures for the synthesis process makes certainly the main difference and winning factor with respect to the LA and AD techniques. The presence of a catalyst used to decompose the carbon-rich molecules (usually a hydrocarbon) allows the lowering of

the temperature well below 1000 °C, whereas the pressure can range from few Torrs to the atmospheric pressure.

This is why CVD can employ different hydrocarbons in any state (solid, liquid or gas), various substrates supporting the metal catalyst and catalysts of different nature. Many different catalysts and hydrocarbons commonly used in CVD processes are listed in table 1.4 [18],[26].

| Carbon Feedstock material | | Substrates | Catalysts | |
|---|---|---|---|---|
| *Solid* | Camphor<br>Naphthalene | | *Solid*[18] | Iron<br>Nickel<br>Cobalt<br>Platinum<br>Palladium<br>Rhodium<br>Gadolinium<br>Lhantanum |
| *Gas* | Acetylene<br>Benzene<br>Ethylene<br>Methane<br>CO<br>(HiPCO) | Silicon<br>Silicon dioxide<br>Quartz<br>Alumina<br>Porous Silicon<br>Zeolite<br>Sapphire<br>MgO | *Vapor* | Ferrocene<br>Cobaltocene<br>Nickelocene |

**Table 1.4**     Main feedstock gases, substrates and catalysts used in CCVD process for CNTs synthesis.

MWNTs are typically produced using acetylene [27], ethylene [28] and methane [29] while SWNTs are grown using benzene [30], acetylene [31], ethylene [32] and methane [33]. A simple scheme of a typical CVD process involves the flow of a gaseous hydrocarbon in the tube reactor, where the metal catalyst on the supporting substrate is heated at a temperature ranging between 600 and 1200 °C. Hydrocarbon decomposes with the help of the temperature and catalyst.

CVD is a widespread process in the semiconductor industry, therefore CNTs production will easily be scaled up making this process very attractive for a large scale production of nanotubes. Large quantities of MWNTs (~100g/day), by using acetylene, and nanoporous materials as well as SWNTs (~10 g/day), by using HiPCO technique, have been produced respectively by E. Couteau [34] and R. Smalley groups [35].

The processes of formation of both SWNTs and MWNTs are quite different occurring in different temperatures ranges. In particular, MWNTs are grown at lower temperatures producing more defective tubes due to the lacking thermal energy required for the formation of perfect crystalline structures.

# References

[1]     M. S. Dresselhaus, G. Dresselhaus and P. C. Eklund, *Science of fullerenes and Carbon Nanotubes*, Academic Press (1996).

[2]     P. Mauron, *Growth Mechanism and Structure of Carbon Nanotubes*, Ph.D Thesys 2003.

[3]     Y. Wu, B. Yang, B. Zong, H. Sun, Z. Shen and Y. Feng, *J. Mat. Chem.* **14**, 469 (2004).

[4]     R. Tycko, R. C. Haddon, G. Dabbagh, S. H. Glarum, D. C. Douglass and A. M. Mujsce, *J. Phys. Chem.* 95, 518 (1991).

[5]     R. D. Johnson, D. S. Bethune and C. S. Yannoni, *Accounts of Chem. Res*. **25**, 169 (1992).

[6]     S. Iijima, *Nature* **354**, 56 (1991).

[7]     C. Journet and P. Bernier, *Appl. Phys. A: Mater. Sci. Process.* **67**, 1 (1998).

[8]     R. A. Jishi, L. Venkataram, M. S. Dresselhaus and G. Dreselhaus, *Phys. Rev. B* **51**, 11176 (1995).

[9]     M. S. Dresselhaus, G. Dresselhaus and R. Saito, *Carbon* **33**, 883-891 (1995).

[10]    S. Reich, C. Thomsen and J. Maultzsch, *Carbon Nanotubes – Basic Concepts and Physical Properties*, Wiley-Vch (2004).

[11]    N. W. Ashcroft and N. D. Mermin, *Solid State Physics*, Saunders College Publishing (1976).

[12]    N.Hamada, S. I. Sawada and A. Oshiyama, *Phys. Rev. Lett*. **68**, 1579 (1992).

[13]    R. Saito, G. Dresselhaus and M. S. Dresselhaus, *Phys. Rev. B* **61**, 2981 (2000).

[14]    M. Machon, S. Reich, C. Thomsen, D. Sánchez-Portal and P. Ordejón, *Phys. Rev. B* **66**, 155410 (2002).

[15]    J. C. Charlier, X. Gonze and J. P. Michenaud, *Phys. Rev. B* **43**, 4579 (1991).

[16]    Y. Ando and S. Iijima, *Jpn. J. Appl. Phys.* **32**, L107 (1993).

[17]    H. Kataura, Y. Kumazawa, Y. Maniwa, I. Umezu, S. Suzuki, Y. Ohtsuka and Y. Achiba, *Synt. Met.* **103**, 2555 (1999).

[18]    M. Yudasaka, Y. Kasuya, F. Kokai, K. Takahashi, M. Takizawa, S. Bandow and S. Iijima, *Appl. Phys. A* **74**, 377 (2002).

[19]     D. S. Bethune, C. H. Kiang, M. De Vries, G. Gorman, R. Savoy, J. Vazquez and R. Beyers, *Nature* **363**, 605 (1993).

[20]     T. W. Ebbesen and P. M. Ajayan, *Nature* **358**, 220 (1992).

[21]     T. Guo, M. D. Diener, Y. Chai, M. J. Alford, R. E. Haufler, S. M. McClure, T. Ohno, J. H. Weaver, G. E. Scuseria, and R. E. Smalley, *Science* **257**, 1661 (1992).

[22]     Thess, R. Lee, P. Nikolaev, H. Dai, P. Petit, J. Robert, C. Xu, Y. H. Lee, S. G. Kim, A. G. Rinzler, D. T. Colbert, G. E. Scuseria, D. Tománek, J. E. Fischer and R. E. Smalley, *Science* **273**, 483 (1996).

[23]     Y. Ando, X. Zhao, T. Sugai and M. Kumar, *MaterialsToday* (2004).

[24]     C. Journet, W. K. Maser, P. Bernier, A. Loiseau, M. L. Delachapelle, S. Lefrant, P. Deniard, R. Lee and J. E. Fischer, *Nature* **388**, 756 (1997).

[25]     M. H. Rümmeli, E. Borowiak-Palen, T. Gemming, T. Pichler, M. Knupfer, M. Kalbác, L. Dunsch, O. Jost, S. R. P. Silva, W. Pompe and B. Büchner, *NanoLett.* **7**, 1209 (2005).

[26]     J. W. Ward, B. Q. Wei and P. M. Ajayan, Chem. Phys. Lett. 376, 717 (2003).

[27]     M. Josè-Yacamàn, M. Miki-Yoshida, L. Rendon and J. G. Santiesteban *Appl. Phys. Lett.* **62**, 657 (1993).

[1]     B. C. Satishkumar, A. Govindaraj, C. N. R. Rao, *Chem. Phys. Lett.* **307**, 158 (1999).

[2]     K. Hernadi, A Fonseca, J. B. Nagy, D. Bernaerts, A. A. Lucas, *Carbon* **34**, 1249 (1996).

[3]     H. M. Cheng, F. Li, X. Sun, S. D. M. Brown, M. A. Pimenta, A. Marucci, G. Dresselhaus, M. S. Dresselhaus, *Chem. Phys. Lett.* **289**, 602 (1998).

[4]     B. C. Satiskumar, A. Govindaraj, R. Sen, C. N. R. Rao, *Chem. Phys. Lett.* **293**, 47 (1998).

[5]     J. H. Hafner, M. J. Bronikowski, B. K. Azamian, P. Nikolaev, A. G. Rinzler, D. T. Colbert, K. A. Smith and R. E. Smalley, *Chem. Phys. Lett.* **296**, 195 (1998).

[6]     J. Kong, A. M. Cassel and H. Dai, *Chem. Phys. Lett.* **292**, 567 (1998).

[7]     E. Couteau, K. Hernadi, J. W. Seo, L. Thiên-Nga, C. Mikó, R. Gaál and L. Forró, *Chem. Phys. Lett.* **378**, 9 (2003).

[8]     M. J. Bronikowski, P. A Willis, D. T. Colbert, K. A Smith and R. E. Smalley, *J. Vac. Sci. Thechnol. A* **19**, 1800 (2001).

## 2. *Synthesis of Carbon Nanotubes: Experimental Results*

The aim of this Chapter is to provide a wide and as more complete as possible overview of the main results obtained performing Carbon Nanotubes growth. We will describe the facilities, the experimental methods and the main process steps used to synthesize CNTs samples. We synthesized carbon nanotubes by using a catalytic chemical vapor deposition. In particular all our efforts have been addressed to the implementation of a deposition process able to produce well oriented, isolated and thin CNTs (eventually SWNTs) in well defined positions on the substrate with clean processes. In fact these requirements to the CNTs growth match the purpose of integration of carbon nanotubes in electronic devices. All the synthesis processes have been achieved at the CNR-IMM (Institute for Microelectronics and Microsystems) of the National Research Council of Bologna.

### 2.1 *Synthesis of Carbon Nanotubes: CVD reactor*

All the samples that we will introduce have been grouped in four main categories depending on the properties that as-grown CNTs samples show and that are specific of the examined group. In particular, the specimens we will present in the following belong to the forest-like growth, patterned-growth, self bridging-growth and device-growth groups whose characteristics are summarized in Table 2.2.

In the processes described in this thesis work, CNTs were grown using two CVD systems, a vertical stainless steel reactor and a horizontal quartz tubular furnace whose main characteristics are briefly listed in table 2.1.

– Vertical reactor is a stainless steel chamber provided of an ultra high vacuum pumping system and a throttle valve arrangement that allows operating in the UHV ($< 10^{-7}$ mbar), low pressure (LPCVD) and atmospheric pressure (APCVD) ranges and prepared to develop PECVD processes also. Ar, $N_2$, $H_2$, $CH_4$, $C_2H_2$, $NH_3$ gas lines are enabled to assist the process. The substrates are loaded on the top of a boron nitride heater that can reach up to 1600 °C with a real substrate temperature of 1200 ℃.

– Horizontal reactor is a tube quartz furnace working at atmospheric pressure or in the vacuum range typical of a rotary pumping system range ($\sim 10^{-4}$ torr). The process gases are the same used for the processes in the vertical reactor. The substrates are placed on a quartz shuttle sample holder in the central part of the

tube furnace that can be heated with the help of an external heater up to 1100 ºC.
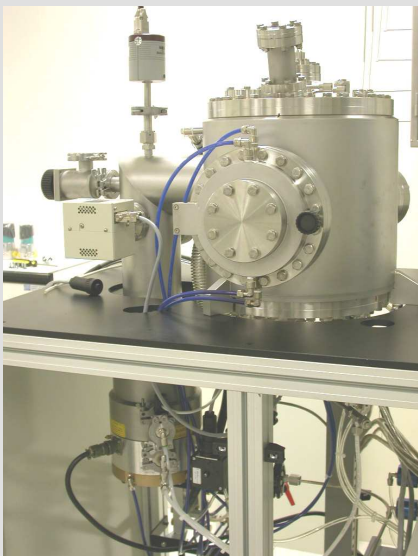
| CVD Vertical Reactor | | | Horizontal quartz reactor | | |
|---|---|---|---|---|---|
| | | | *Front view* | | |
| | | | *Back view* | | |
| Stainless steel reaction chamber | | | Quartz chamber | | |
| *Pressure* | UHV | $10^{-7}$ torr | | LP | $> 10^{-4}$ torr |
| | LP | $10^{-2} \div 100$ torr | *Pressure* | | |
| | AP | 760 torr | | AP | 760 torr |
| *Gas supply* | Ar, $N_2$, $H_2$, $CH_4$, $C_2H_2$, $NH_3$ | | *Gas supply* | Ar, $N_2$, $H_2$, $CH_4$, $C_2H_2$, $NH_3$ | |
| *Flow rates* | $1 \div 1000$ sccm | | *Flow rates* | $1 \div 1000$ sccm | |
| *Temperature* | $\leq 1600$ ºC | | *Temperature* | $\leq 1100$ ºC | |
| *Sample holder* | $100 \times 100$ mm$^2$ | | *Sample holder* | $60 \times 30$ mm$^2$ | |

**Table 2.1**    Main features of horizontal and vertical CVD reactors for CNTs growth.

During a chemical vapor growth there are a large number of key factors and parameters influencing the nanotubes nucleation and growth and a lot of efforts have been spent to clarify them. What are actually the parameters influencing the location,

the growth regimes and rates and the particular kind of nanotubes grown, is not yet clear. In particular the roles of metal catalyst, substrate, feedstock gas and growth parameters are critical to drive the growth process towards a controllable CNTs synthesis. The kind and morphology of the metal catalyst, its interaction with the substrate, the temperature of the feedstock gas decomposition, the formation of a metal-carbon phase after the carbon precipitation into the metal particle, the reaction gases and the reducing or oxidizing role of the carrier gas on the catalyst, are some of the parameters we needed to control and optimize.

In this thesis work the CCVD depositions that have been carried out, have been grouped in four main classes. Here below is shown a synoptic table summarizing the most remarkable growth processes we carried out, in order to evidence the results achieved on the CNTs growth control.

| Deposition | Substrates | Catalyst | $t_{dep}$ [s] | Feedstock gas and process T [°C] | Deposition gas flows [sccm] |
|---|---|---|---|---|---|
| **Forest Growth** | PS1 PS2 S3 S4 | Fe e-gun evaporation | 300 | $C_2H_2$ 700 | $C_2H_2$ (100) (100%) |
| **Patterned Growth** | S SO OxPS | Fe e-gun evaporation | 600 | $CH_4, H_2$ 900 | $CH_4$(140) : $H_2$ (16) (92%) |
| | | | 600 | $CH_4$ 900 | $CH_4$ (140) (100%) |
| **Self Bridging Growth** | S SO Poly-S | Fe e-gun evaporation / $Fe(NO_3)_3 \cdot 9H_2O$ + isopropyl alcohol | 600 | $CH_4$ 900 | $CH_4$ (140) (100%) |
| **Device Growth** | S/SO/Poly S/SO/T S/SO/T/TN | $Fe(NO_3)_3 \cdot 9H_2O$ + isopropyl alcohol | 600 | $CH_4$ 900 | $CH_4$ (140) (100%) |

**Table 2.2**    Main characteristics of the four group of CNTs deposition processes analyzed in the follow.


The acronyms S, PS, SO and OxPS indicate respectively Si, nano-porous Si, Si oxide and oxidized porous Si substrates. The 1 and 3 numbers indicate Fe coated substrates that underwent an overnight oxidation process in air at 300 °C while 2 and 4 indicate substrates without oxidation.

All CNTs growth processes have been implemented in these two reactors changing the operating conditions, in order to obtain the desired control on the

nanotubes features, location, alignment and type. The guideline of the work is connected with the achievement of a control on the growth of the carbon nanotubes. This goal has been accomplished by considering different aspects and improvements, such as more defined and controlled process steps, a control on the location of the catalyst, as well as the alignment and type or nature of the deposited carbon nanotubes.

## 2.2       *Growth of Carbon Nanotubes on silicon and porous silicon substrates: Forest-like growth*

Large amount of multiwall carbon nanotubes can be easily obtained by using carbon feedstock materials that require a low dissociation temperature. This is the case, for example, of acetylene that easily decomposes at 700 ºC on a bare substrate leaving a residue of amorphous carbon. To implement the synthesis of carbon nanotubes the use of a catalyst in form of nanoparticles is needed in order to allow the formation of carbon nanotubes. In the present case we started by developing a synthesis process where an iron layer, few nanometers thick, was deposited on a substrate.

In particular, silicon and nano-porous silicon substrates have been used. All substrates are covered with thin iron films evaporated on the top of the wafers through a shadow mask to pattern macroscopic catalyst areas. Acetylene chemical vapor growth was then performed using the vertical reactor in an argon atmosphere. Carbon nanotubes resulting from this process consist of densely packed bundles, vertically aligned on the length scale of several microns, with the filament length ranging from several tens to hundreds of microns, as well as randomly oriented bundles, depending on the selected substrate. Because of the high density of such bundles this kind of growth is called forest like growth. In the following we report some details of this kind of growth.

### 2.2.1 Substrates selection and metal catalyst coating

The substrates employed for this process were Si (S) and Nano-porous Si (PS). Nano-pores structure was obtained on (100) $n^+$ Si (CZ) wafers, (dopant As, resistance lower than 0.007 ohm), by electrochemical etching in an isopropyl alcohol solution of hydrofluoric acid, for 5 min at a current of 3 A. In these conditions the thickness of

the layer is around 4 μm. A very thin native Si-oxide layer of about $1 \div 2$ nm is formed when Si is in contact with air.

The iron used as a catalyst and metal coating was obtained by mounting the samples in a planetary of a vacuum e-gun evaporation system. The growth rate selected for the process is about 5 Å/s. In order to test the patterning of the growth and hence start to localize the CNTs growth, as described in the guidelines above, the samples were deposited with iron by using a shadow mask with circular dots of different diameters i.e., 500, 750, 2500 μm. A simple scheme of the dots distribution is showed in figure 2.2.1. In this way it is compared the growth both on patterned and not patterned substrates.
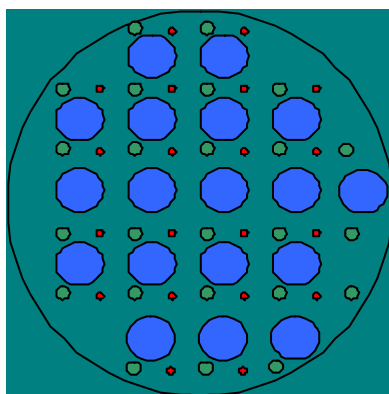


**Fig. 2.2.1**    Scheme of the circular dots in the shadow mask used to evaporate the catalyst. Red, green and blue dots correspond to 500, 750 and 2500 μm respectively.

A thickness monitor controls the catalyst layer thickness to obtain a uniform metal film about 5 nm thick. A summary of Fe - coated samples is reported in table 2.3.

| Samples Name | Substrates | Evaporation time [s] and Fe Thickness [Å] | | Overnight Oxidation |
|:---:|:---:|:---:|:---:|:---:|
| PS1 | Porous Si | 10 | 50 | Yes |
| PS2 | Porous Si | 10 | 50 | No |
| S3 | Si | 10 | 50 | Yes |
| S4 | Si | 10 | 50 | No |

**Table 2.3**    Substrates, Fe evaporation time and thickness and oxidized state of samples.

Some iron deposited samples underwent an overnight oxidation in air at 300 ºC. The oxidation process could enhance the formation of an oxidized Fe phase useful for the hydrocarbon dehydrogenation and C precipitation through the catalyst particle.

### 2.2.2 Chemical Vapor Deposition of Forest-like Carbon Nanotubes

CNTs depositions have been accomplished in the CVD vertical reactor setting growth parameters as indicated in the flowchart below. The feedstock gas for the growth is acetylene and all the processes are developed using argon as carrier gas. In the starting conditions the chamber is pumped at $10^{-7}$ torr, and then Ar gas is introduced to test the reactor vacuum state. After reaching the atmospheric pressure, the heater is switched on, ramping up to 1000 °C, corresponding to a substrate temperature of about 700 °C.

Samples are then kept at 700 °C for five minutes in argon flow after that the argon is switched off and acetylene is introduced in the chamber. Following this catalytic deposition step, acetylene flow is interrupted and the samples are kept for few minutes at the deposition temperature in argon flow only.

| Deposition parameters: forest – like growth | | | | | |
|---|---|---|---|---|---|
| System state | Process step | Pressure [torr] | Heater Temperature [°C] | Time [s] | Process gas flow [sccm] |
| Stand by Step 0 | RAMP UP HEATING | 760 | R.T. | | 500, Ar |
| Step 1 | | 760 | 200 | 300 | 500, Ar |
| Step 2 | | 760 | 400 | 300 | 500, Ar |
| Step 3 | | 760 | 600 | 300 | 500, Ar |
| Step 4 | | 760 | 800 | 300 | 500, Ar |
| Step 5 | | 760 | 1000 | 300 | 500, Ar |
| Step 6 | Intermediate state | 760 | 1000 | 300 | 150, Ar |
| Step 7 | DEPOSITION | 760 | 1000 (700) | 300 | 100, $C_2H_2$ |
| Step 8 | PURGE | 760 | 700 | 180 | 150, Ar |
| Step 9 | | 760 | 400 | 300 | 150, Ar |
| Step 10 | | 760 | 100 | 600 | 150, Ar |
| Step 11 | | 500 | 25 | 300 | 150, Ar |
| Step 12 | Rapid stop | 200 | 25 | 300 | 150, Ar |
| Step 13 | Last Step | 0.1 | 25 | 300 | 150, Ar |

**Table 2.4**     Flowchart of the growth process for forest like growth of patterned and not patterned, oxidized and non oxidized silicon and porous silicon substrates.


The deposition step is followed by a quite fast ramping-down of the system passing from 700 ºC to room temperature by only using argon flow. The last steps of the process have been carried out reducing the operating pressure and samples have been unloaded after venting the chamber.


### 2.2.3 SEM characterization of as-grown samples

All the grown samples were inspected by using the scanning electron microscopy (SEM) as a standard technique. A visual observation preliminary to the

SEM analysis shows a dark grey layer covering the catalyst patterned islands. The SEM images of selected sample areas have been collected using a planar and 40 or 45 degree tilted stub at different magnifications and they have been grouped for both PS1 and S3 samples. In the following some typical results obtained are reported.

Six micrographs for the case of PS1 sample, taken on three different dots having a diameter of 500, 750 e 2500 µm respectively, are reported in fig. 2.2.2 at low and high magnification.
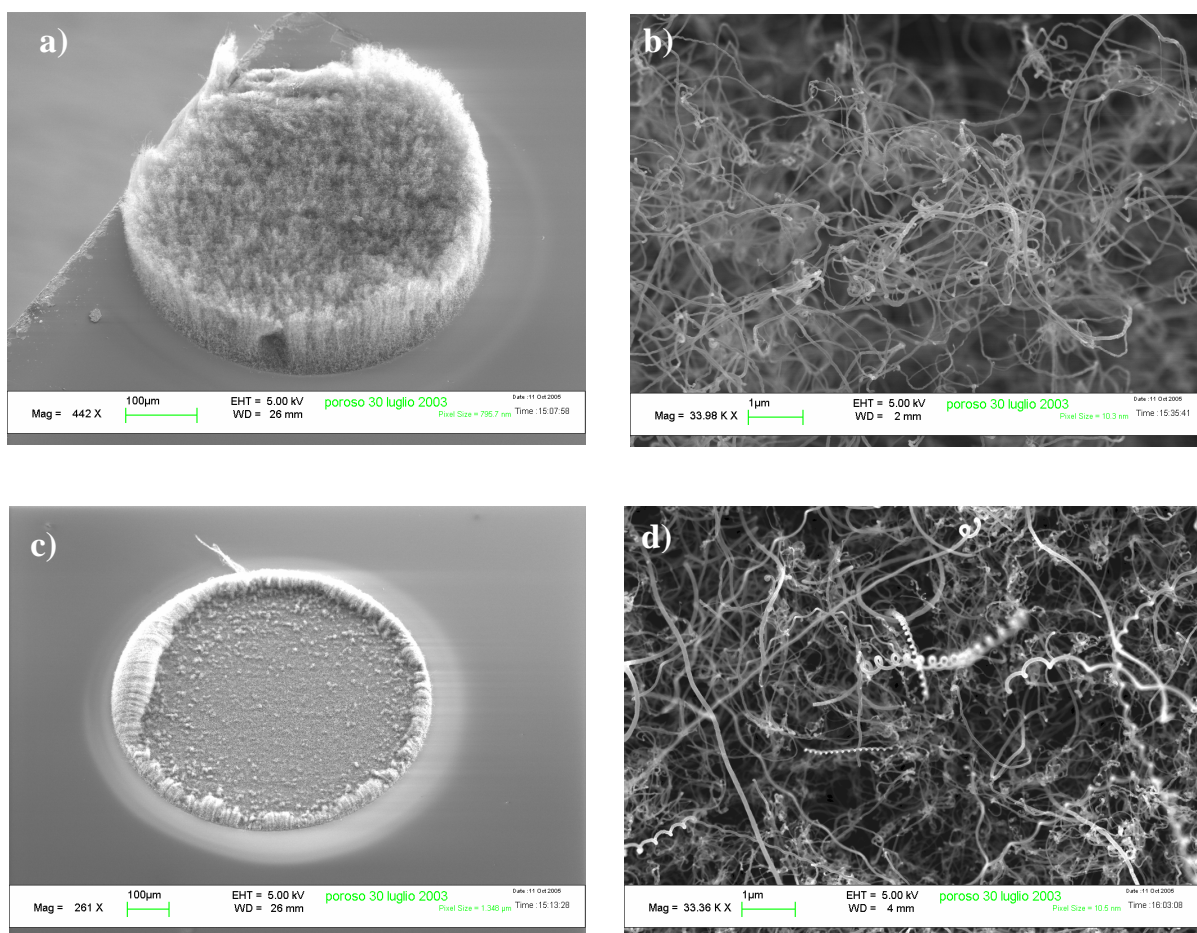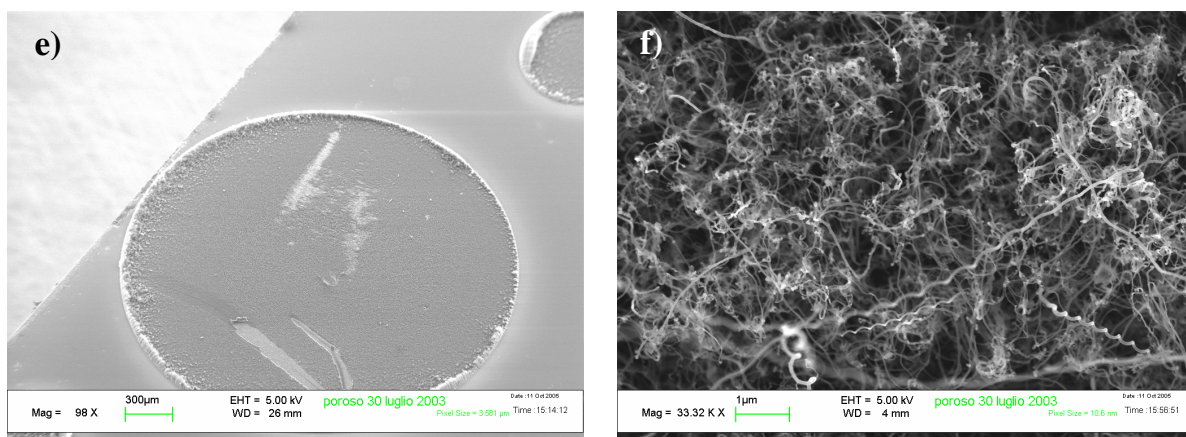
**Fig. 2.2.2**    SEM micrographs of CNTs grown on 5 nm Fe layer (dot), evaporated by e-gun on a nanoporous Si substrate and after the oxidation process in air. **a)** Tilted top view and **b)** high magnification of the center of the 500 µm large dot. **c)** Top view and **d)** high magnification of the center of the 750 µm large dot. **e)** Top view and **f)** high magnification of center of the 2500 µm large dot.

The SEM micrographs of the three dots (500 µm, 750 µm, 2500 µm) reported in fig. 2.2.2 a), c) and e), show how the homogeneity in nanotubes nucleation is not respected over all the dots. In particular, on the smallest dot, CNTs grow as entangled structures, vertically aligned with respect to the substrate, uniformly distributed over all the patterned area. Fig. 2.2.2 c) and e) show how a different growth regime is established over larger dots. In particular, it does exist a circular ring where bundles of CNTs have grown while keeping the same height and density. It also exists an internal circumference where nanotubes have grown with the same morphology but shortest bundles.

The high magnified images collected at the center of the different dots (see fig. 2.2.2 b), d) and f)), show how the CNTs form entangled bundles with some coiled nanotube with a decreasing density when moving from 2500 µm to 500 µm wide dot. This could be related to the largest amount of catalyst on the widest dots (750 µm and 2500 µm) leading to the nucleation of more dense bundles of nanotubes.

Among the 500 µm dots, different growth regimes are observed. Fig 2.2.3 evidences three 500 µm dots placed in different substrate positions with respect to the

edges, evidencing the same phenomenon of a pronounced growth in the circumferential ring. This effect is gradual in the four dots shown in fig. 2.2.3.
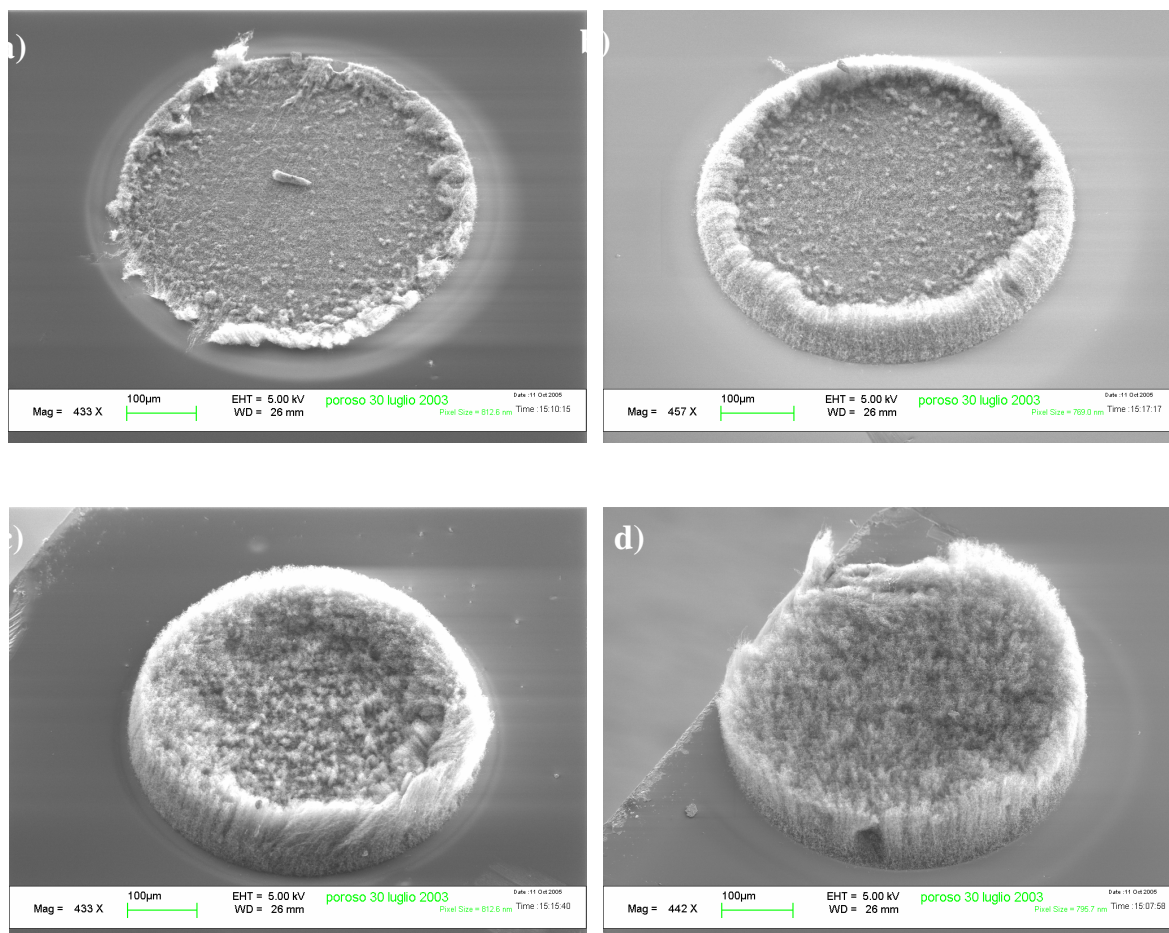


**Fig. 2.2.3 a) – d)**  SEM micrographs of CNTs grown on the same sample on 5 nm Fe dots, 500 µm large. An inhomogeneous growth mechanism is observed.

The difference in the density of CNTs bundles nucleated over the dots having the same dimension, is highlighted in fig. 2.2.3. Moving from fig. 2.2.3 a) to b) the circular ring, where the bundles of nanotubes are visible, looks enlarged up to be quite uniform over the whole dot as shown in fig. 2.2.3 d). These non uniform densities over the dots could be attributed to the combination of a temperature non uniformity over the entire dot as well as to a difference in the thickness of the catalyst layer passing from the border to the center of the dot and from a dot to another one. These non uniformity effects are enhanced by pores that act as channels guttering acetylene

along preferential paths in the substrate and leading to a complementary feedstock source for the CNTs nucleation [1].

In order to evidence the influence determined by the porous structure of PS, the previous result is compared with that obtained by performing a deposition under the same conditions, on a flat Si substrate. In figure 2.2.4 SEM micrographs of plane silicon samples after the oxidation process have been reported. The micrographs have been collected on the dot areas.

**Fig. 2.2.4**  SEM micrographs of CNTs on 5 nm Fe layer dots evaporated on a (100) Si substrate by e-gun and oxidized in air (sample S3). **a)** Tilted view of the dot and **b)** higher magnification of the CNTs grown at the dot edge (top view). **c)**, **e)** and **g)** top views of 500, 750 and 2500 µm wide dots while **d)**, **f)** and **h)** high magnification of 500, 750 and 2500 µm wide dots.
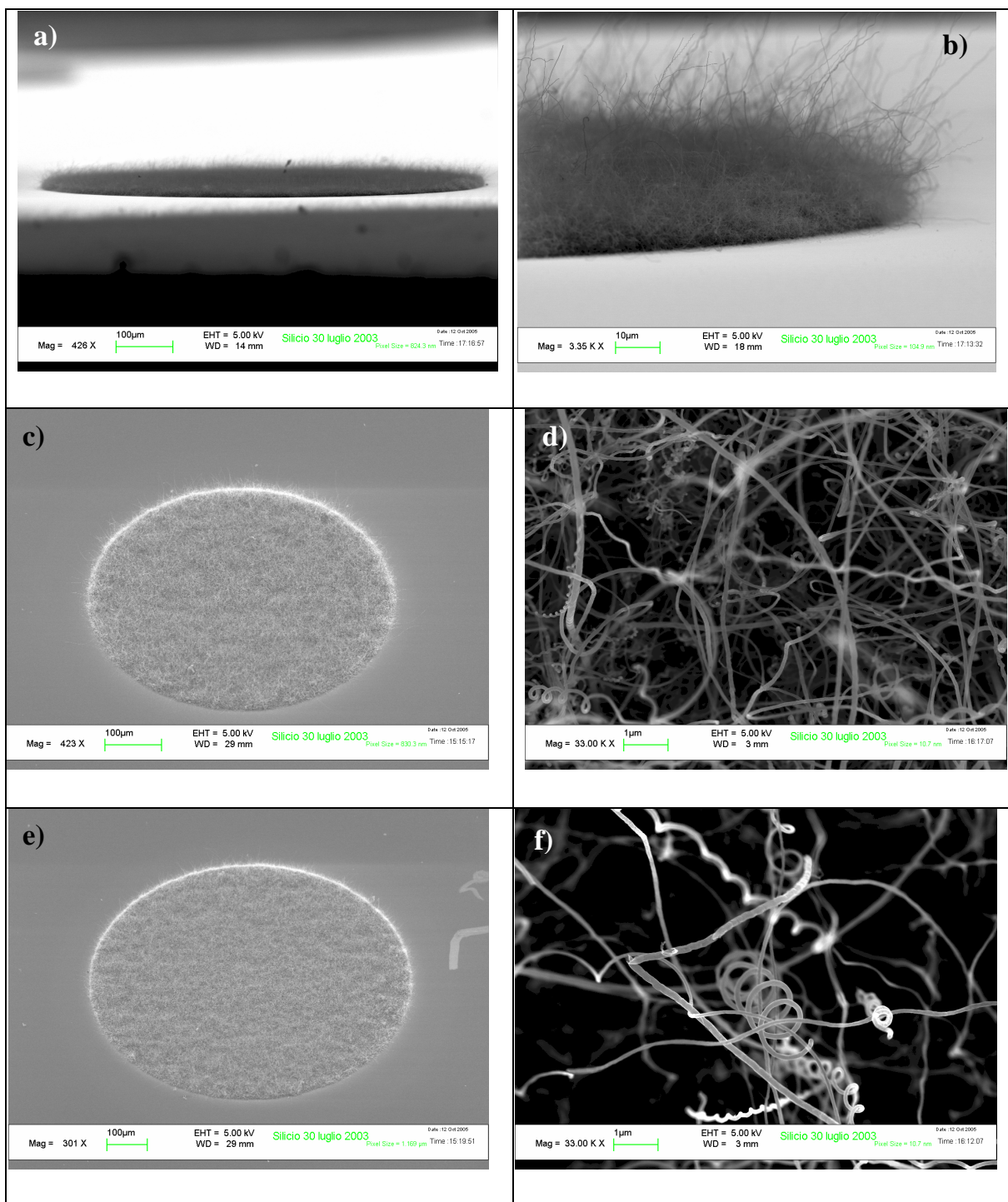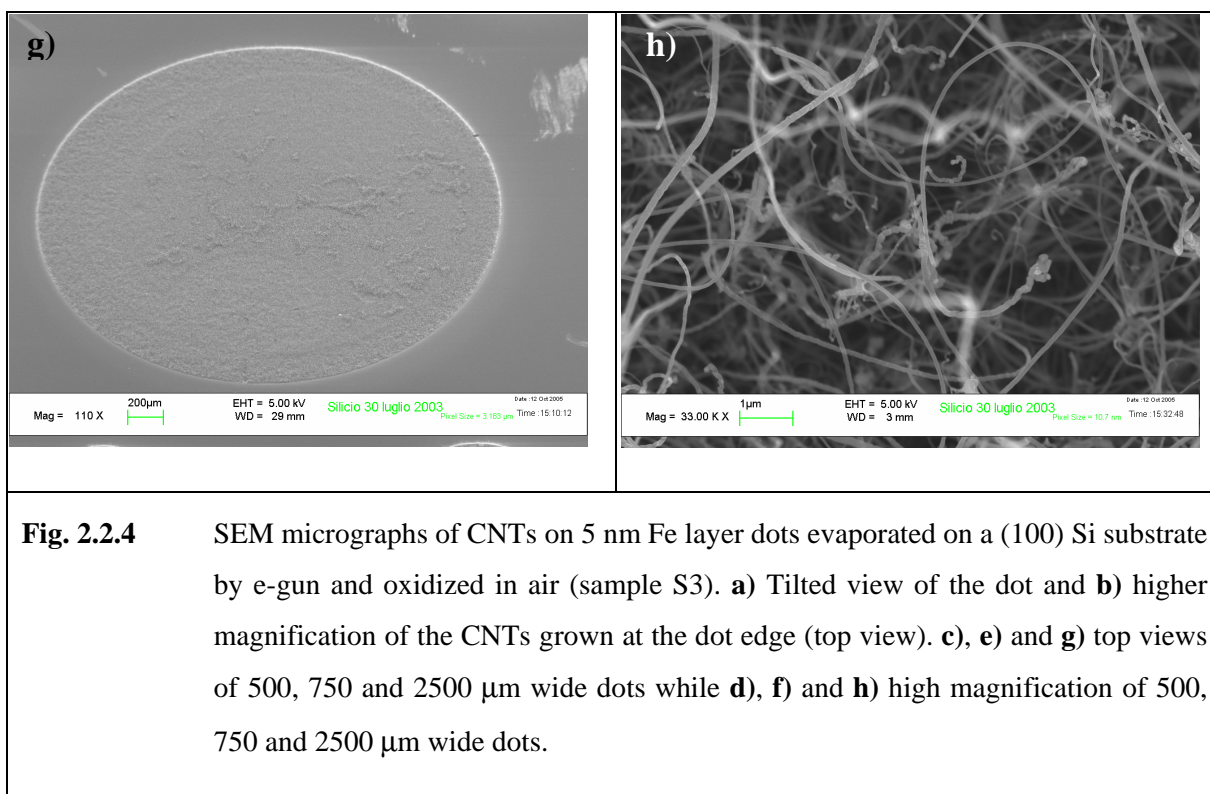
The evidences reported for the growth of carbon nanotubes on silicon and porous silicon show strong differences between the two cases highlighting as the substrate and, in particular, its porosity, has an influence on the growth process of carbon nanotubes. Moving from the smallest (500 µm) to the largest dot (2500 µm) on silicon substrates, the growth of CNTs looks uniform over the whole dot. The CNTs look like bundles of randomly oriented structures not as long as in the case of PS substrates. The density of bundles on the dots of different dimensions is comparable. Comparing PS and S substrates is possible to conclude that the non uniformity of bundles on porous silicon is strongly influenced by the morphology of this substrate and by the guttering action of the pores.

In figure 2.2.5 are reported the SEM micrographs of Si and porous Si substrates with Fe that went through the annealing (oxidation) process (S3, PS1) or not (S4, PS2) in order to compare the oxidation effect on the two different substrates.

**Fig. 2.2.5**    SEM micrographs of bundles of CNTs on **a)** oxidized Fe on porous silicon (PS1), **b)** non oxidized Fe on PS (PS2), on **c)** oxidized Fe on silicon (S3), **d)** non oxidized Fe on silicon (S4). The insets of a) and c) show higher magnification micrographs of the CNTs entangled bundles.
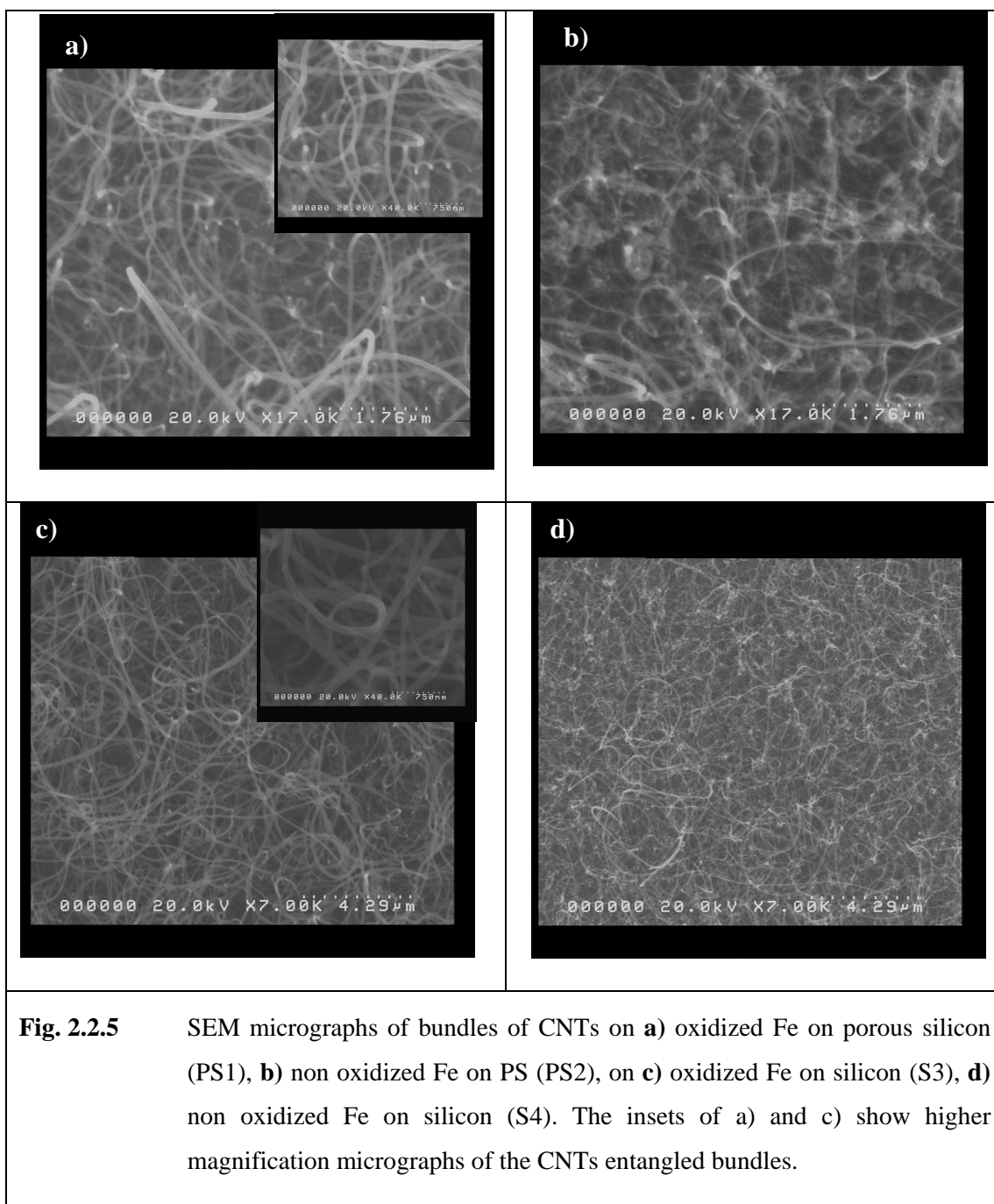
CNTs grown on oxidized and not oxidized Fe/substrates have different densities and diameters. Nanotubes grown on oxidized S and PS substrates are less dense than that grown on non oxidized substrates. Bundles of CNTs on PS substrates have smaller diameters than that on S substrates. It is possible to observe as the oxidation process give rise to a better fragmentation of Fe-NPs corresponding to the nucleation of smaller nanotubes. The smallest diameters of CNTs grown on PS could be due to the pinning effect of pores on the Fe-NPs that limits the phenomenon of catalyst aggregation.

Similar results have been obtained in the case of S and PS substrates without patterned dots where CNTs nucleate everywhere on substrate surface.

### *2.2.4 Summary*

- CNTs on PS grow only on the dots where catalyst is evaporated while there is no evidence of CNTs and amorphous carbon out of the dots **(see Fig. 2.2.2)**.

- The micrographs evidence the presence of a 100 µm structure protruding perpendicularly to the surface of the dot on PS. A higher magnification of this cylindrical structure shows the presence of fibers growing upwardly in an entangled form **(see Fig. 2.2.2)**.

- The dots of 500 µm show differences in the uniformity of the CNTs ranging from the case of uniform CNTs covering the dot to a growth that occurs with different rates along the circular ring around the dot and at the dot center. The 750 and 2500 µm dots show always an external circular ring with longer bundles of CNTs and short bundles in the internal part of the dot **(see Fig. 2.2.2** and **2.2.3)**.

- The growth on PS substrates occurred in 5 minutes with an average length of 100 µm. As a consequence, the average growth rate is about 20 µm/min = 330 nm/sec. However, because of the entangled structure, the real length of a nanotube is greater. If we estimate that the bending reduces of about a factor of 3 the total length of the entangled structure, we have that the length is about 1000 nm/s. This means that the growth process in PS is a quite abrupt growth.

- CNTs on porous silicon are denser, longer and vertically aligned on about 20 µm scale, while CNTs growing on flat silicon substrates are shorter and randomly oriented with respect to the substrate. The three 500, 750 and 2500 µm wide dots on Si show a high density uniformity and CNTs there grown show comparable diameters **(see Fig. 2.2.4)**.

- Because the evaporation process of the Fe catalyst, the oxidation step and deposition run are the same for both the Si and PS substrates, we can conclude that the substrate is now playing a fundamental role in the selection of growth mechanism (entangled vertical structures or randomly oriented CNTs). This suggests that the entangled vertical structures obtained on PS are connected with the aptitude of the carbon containing gas ($C_2H_2$) in finding diffusion paths in the porous substrate,

thus increasing the carbon feedstock to the growing structure, as also considered by Fan et al. [1].

- CNTs on oxidized samples are less dense and larger than that grown on non oxidized substrates. The bundles of CNTs have larger diameters on silicon than PS, where the effect of Fe oxidation seems to be less pronounced **(see Fig. 2.2.5)**. We speculate that the oxidation process forms iron oxide giving rise to particles of larger sizes.

### *2.3 Growth of Carbon Nanotubes on micro patterned substrates of silicon, silicon oxide and porous silicon*

In the previous paragraphs we described as entangled vertical structures of CNTs are obtained in an explosive growth process on porous Si and as bundles of randomly oriented CNTs on Si. However, the common result is that the location of the catalyst gives a control on the localization of the nucleation process that starts the growth. This can determine the localization of the growth of carbon nanotubes. For this reason, in order to orient the CNTs growth process towards the large scale integration process of the microelectronic industry, a suitable reduction of the patterns on which CNTs can be grown must be achieved.

A further step to improve the control of nanotubes position is to design suitable substrates, useful to match this goal. We manufactured patterned structures having minimum geometries of micron size, by means of the standard lithographic technique. The localization of the catalyst in the micron scale was achieved in this case by implementing the lift-off technique of the resist after the evaporation of the catalyst layer. In particular, the substrates that we employed were covered with few nanometers of evaporated iron on micrometric patterned areas and after that the resist was lifted-off.

Afterward, all the substrates underwent deposition processes performed in the tubular quartz reactor described above. We used methane ($CH_4$) as the feedstock gas and argon or hydrogen for the annealing atmosphere. The choice of methane as the carbon feedstock gas is connected with the fact that our experimental findings in the case of growth by using acetylene showed that, as a consequence of the lower decomposition energy required for this gas, a large amount of amorphous carbon can be produced along with the CNTs. Hence, in order to achieve a growth control of the
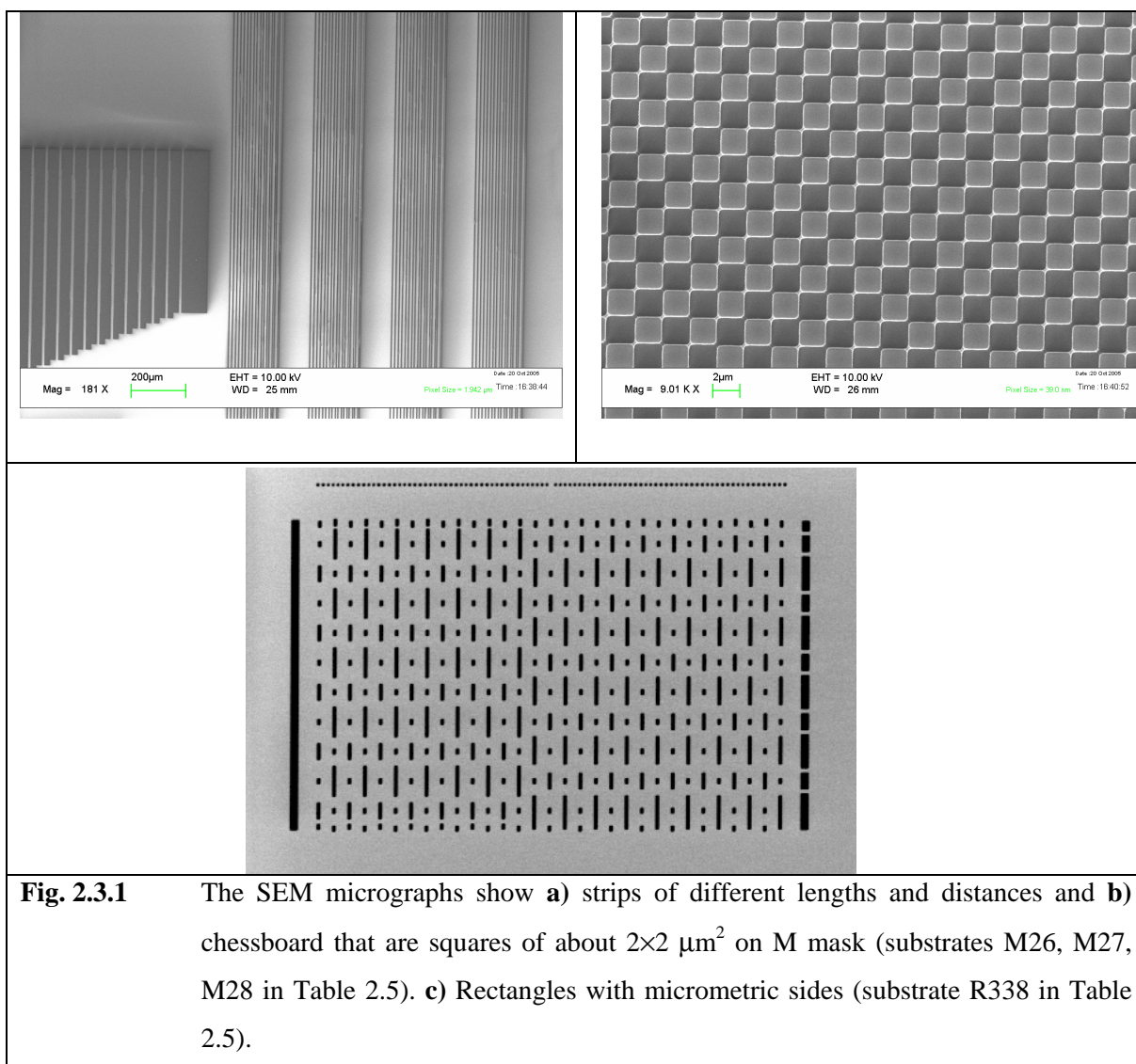
CNTs, we first investigated the effect of the gases in various steps of the deposition processes. In the following, we present four deposition processes only differing for the gases assisting the ramp-up and annealing steps and the deposition process.

In the specific, in the first case argon was used both in the rump-up and annealing processes. In the second case, Ar was inserted in the rump-up and hydrogen in the annealing and deposition steps. In the third case, $H_2$ was also flown in the ramping-up. In the fourth case, we maintained all the gasses and switched off the $H_2$ during the deposition process. All the parameters used during the process are summarized in table 2.5. The last process, with the deposition in pure methane, gave the best results in order to gain, in our experimental conditions, a control on the growth process.

### 2.3.1 Substrates selection and metal catalyst coating

The substrates employed for this process were oxidized PS (OxPS) having the same characteristics described in the paragraph 2.2.1, Si and $SiO_2$ (SO) obtained by means of the thermal oxidation process. In particular $SiO_2$ 90 nm thick was grown on silicon wafers ((100), p type) by using the well established processes of steam oxidation at 1000 ºC. Different types of substrate and processing will be indicated in the following with the id number of the wafers, i.e. 26 for OxPS, 27 and 338 for SO and 28 for S substrates.

With the aim of shrinking and further locate the CNTs structures, we used a lift-off method. More precisely, a set of windows, microns wide, have been opened on a resist layer. After that the iron metal catalyst is evaporated and with a removal process using microstripper developer, a set of catalyst strips and islands are left on the substrate. Some structures of the two mask used, are shown in fig. 2.3.1.

**Fig. 2.3.1**    The SEM micrographs show **a)** strips of different lengths and distances and **b)** chessboard that are squares of about $2\times2$ $\mu m^2$ on M mask (substrates M26, M27, M28 in Table 2.5). **c)** Rectangles with micrometric sides (substrate R338 in Table 2.5).

Iron films were evaporated at a growth rate of 5 Å/s for 4 and 2 s, giving 1 nm and 2 nm thick films, respectively. A subsequent lift-off process leaves on the substrate square and strips covered with the evaporated catalyst. The samples analyzed are resumed in the table 2.5.

| Samples Name | Substrates | Evaporation time (s) and Fe Thickness (Å) | | Gas | | | |
|---|---|---|---|---|---|---|---|
| | | | | Ramp up | Annealing | Depos. | Ramp down |
| M26C1 | OxPS | 4 | 20 | Ar | Ar | $H_2$, $CH_4$ | Ar |
| M27C1 | SO | | | | | | |
| M26C2 | OxPS | 4 | 20 | Ar | $H_2$ | $H_2$, $CH_4$ | $H_2$ |
| M27C2 | SO | | | | | | |
| M26C3 | OxPS | 4 | 20 | $H_2$ | $H_2$ | $H_2$, $CH_4$ | $H_2$ |
| M28C3 | S | | | | | | |
| M26C4 | OxPS | 4 | 20 | | | | |
| M26A4 | OxPS | 2 | 10 | | | | |
| M27C4 | SO | | | $H_2$ | $H_2$ | $CH_4$ | $H_2$ |
| M27A4 | SO | 4 | 20 | | | | |
| R338A4 | SO | 2 | 10 | | | | |
| M28A4 | S | | | | | | |

**Table 2.5**   The substrate type, the evaporation time of the catalyst with its nominal thickness, the gases used during the different steps of the whole process, are reported.

The evaporation processes leading to 2 and 1 nm thick Fe films, are indicated with the letters C and A, respectively. Catalyst doesn't undergo an overnight oxidation process, in order to leave smaller catalyst nanoparticles on the substrate for the nucleation of smaller diameter tubes (as shown by the results obtained in the Par.2.2.3). The last number in the name of the samples is reserved to the adopted deposition process (see tables 2.6 and 2.7).

## 2.3.2 Chemical Vapor Deposition of Carbon Nanotubes on micro patterned substrates

The CVD deposition processes of CNTs have been carried out in a horizontal tube quartz furnace. The methane is used as feedstock gas because it decomposes to higher temperatures (900 ºC) leaving substrates clean from amorphous carbon and because it is compatible with the nucleation of single wall nanotubes. The growth of carbon nanotubes was investigated by performing four different deposition processes where the effects of Ar and $H_2$ are studied as well as the best methane concentration. We started by setting a dilution percentage of $CH_4$ in $H_2$ in the range reported in literature as the best one (91% ÷ 94%) for CVD SWNTs synthesis without amorphous

carbon deposit (the so-called growth regime) [2]. The best deposition conditions were obtained by optimizing case by case each gaseous species involved in the ramp-up, annealing deposition and ramp-down steps, respectively. Passing from process 1 to process 2, the annealing gas was changed from Ar to $H_2$. The hydrogen leaves the surface cleaner, without sensible change in the grown nanotubes on OxPSi, differently from the case of the SO substrates, where the switch from Ar to $H_2$ enhances the nanotubes nucleation. In process 3 we changed the gas of ramp-up and ramp-down from Ar to $H_2$. Smaller diameter and longer nanotubes were obtained with this process. Moreover, with respect to the case of argon, the use of $H_2$ resulted in activating more nanoparticles on the patterned islands and enabling a higher density of CNTs nucleation sites. Because of the stronger fractioning effect of the $H_2$ on the metal nanoparticles (Me-NPs), we clearly preferred the use of this gas in the processes we implemented further.

The steps of the four deposition processes here presented are collected in the flowcharts reported in table 2.6 and 2.7, where the only differences are in the gas and flow settings, i.e. the last two columns.

| Deposition parameters: micropatterned growth | | | | | Process 1 | Process 2 |
|---|---|---|---|---|---|---|
| System state | Process step | Pressure [torr] | Heater Temperature [°C] | Time [s] | gas flow [sccm] | |
| Stand by Step 0 | RAMP UP HEATING | 760 | R.T. | 600 | 1000, Ar | 1000, Ar |
| Step 1 | | 750 | R.T. | 600 | 200, $H_2$ | 200, $H_2$ |
| Step 2 | | 750 | R.T. → 860 | 3600 | 200, Ar | 200, Ar |
| Step 3 | **ANNEALING** | 750 | 860 | 1200 | 200, Ar | 16, $H_2$ |
| Step 4 | **DEPOSITION** | 750 | 860 (900) | 600 | **140, $CH_4$ 16, $H_2$** | **140, $CH_4$ 16, $H_2$** |
| Step 5 | PURGE | 750 | 700 → R.T. | *overni ght* | 200, Ar | 200, Ar |

**Table 2.6**    Flowchart of different steps and values of the deposition parameters of process 1 and 2.

| Deposition parameters: micropatterned growth | | | | | Process 3 | Process 4 |
|---|---|---|---|---|---|---|
| System state | Process step | Pressure [torr] | Heater Temperature [°C] | Time [s] | gas flow [sccm] | |
| Stand by Step 0 | RAMP UP HEATING | 760 | R.T. | 600 | 1000, Ar | 1000, Ar |
| Step 1 | | 750 | R.T. | 600 | 200, $H_2$ | 200, $H_2$ |
| Step 2 | | 750 | R.T. $\rightarrow$ 860 | 3600 | 200, $H_2$ | 200, $H_2$ |
| Step 3 | **ANNEALING** | 750 | 860 | 1200 | 16, $H_2$ | 16, $H_2$ |
| Step 4 | **DEPOSITION** | 750 | 860 (900) | 600 | **140, $CH_4$** **16, $H_2$** | **140, $CH_4$** |
| Step 5 | PURGE | 750 | 700 $\rightarrow$ R.T. | *overnight* | 200, $H_2$ | 200, $H_2$ |

**Table 2.7**      Flowchart of different steps and values of the deposition parameters of process 3 and 4.

In the process 4 we left all parameters as set in the process 3 only switching off the $H_2$ during the growth step. This procedure was aimed to avoid the observed damaging of Si substrates following a $H_2$ assisted deposition process as we will show in the following section (Par.2.3.3).

After an overnight cooling in the tube-chamber the samples were unloaded and their morphology analyzed with the SEM.

### 2.3.3 SEM characterization of as-grown samples

The first sample presented is the M26C1. It is an OxPS substrate where two nanometers of iron have been evaporated. Carbon nanotubes synthesis has been performed by using $H_2$ and $CH_4$ during the deposition. In fig. 2.3.2 a SEM micrograph of this sample is reported.
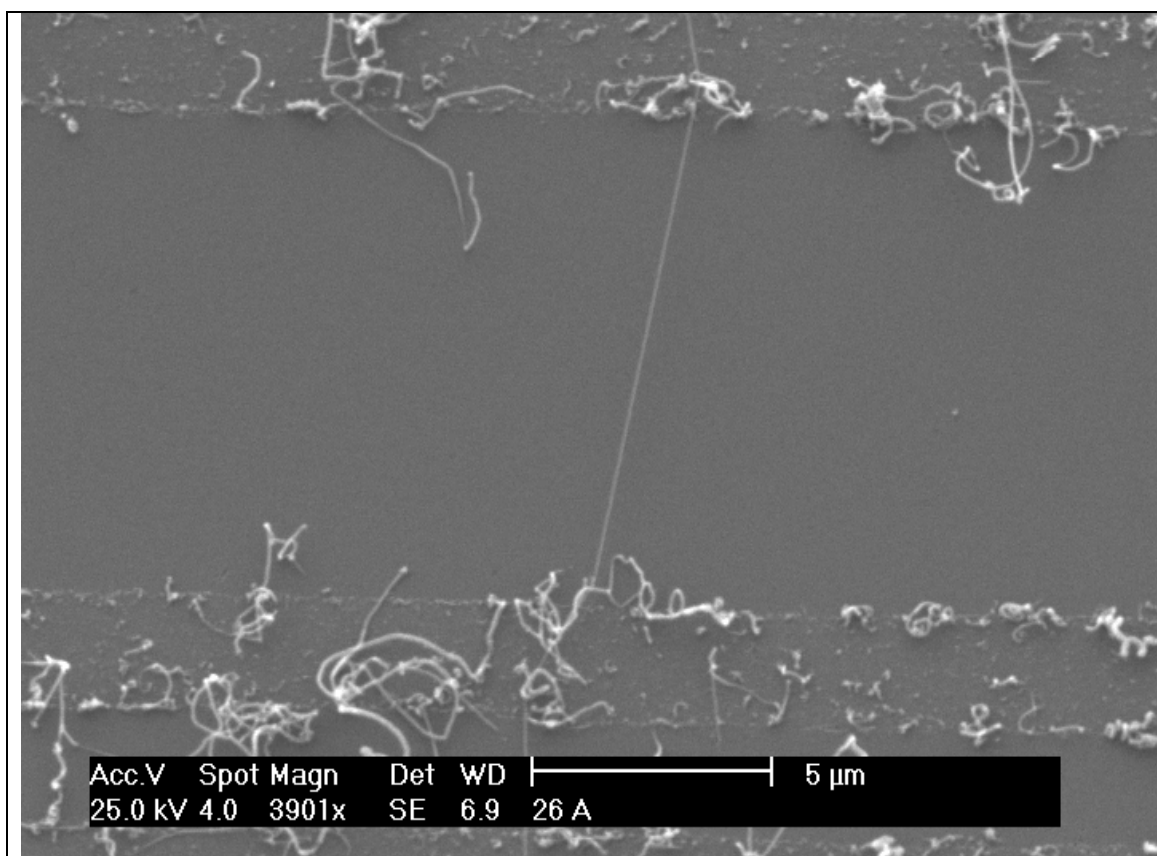
**Fig. 2.3.2**       SEM micrograph of CNTs grown on OxPS substrate with a Fe layer 2 nm thick (M26C1).

The micrograph shows a single nanotube bridging across two stripes of catalyst separated of about 10 µm. This kind of growth is compatible with the "kite-mechanism" [4]-[5]-[7] as it has been shown in the Chap.V. This mechanism proposes the fluctuation of the Fe-NP at the tip of the growing tube in the flux of gases assisting the growth. The nanotube elongation mechanism is stopped when the catalyst nanoparticle comes into contact with the substrate. Some of the impurities of substrate surface poison the Fe-NP during its skidding on the substrate. This reduces the iron catalytic action determining the end of nanotube growth. The result showed in the fig. 2.3.2 is a typical result of the growth of carbon nanotubes on micropatterned substrates. This kind of growth matches well with our purpose of control over the nanotubes orientation, localization and density. This is the reason why we have implemented this kind of process varying the gas mixture to decrease the amount of impurities on the patterned areas. On the micropatterned stripes of catalyst, in fact, we can observe the nucleation of CNTs arrested in an embryonic phase just after the nucleation step. To avoid the nucleation of these spurious structures we tried to

modify the combination of gases assisting all the deposition steps as shown in the four tested processes summarized in table 2.5 that we will describe in the following.

Micrographs of fig. 2.3.3 compare the processes 1 and 2 performed on OxPS and SO substrates. In fig. 2.3.3 a) and b), we show nanotubes grown on OxPS substrates by using process 1 and 2. The two samples are similar with CNTs of about the same length.  In fig. 2.3.3 c) and d) we show nanotubes grown on SO substrates by using process 1 and 2.
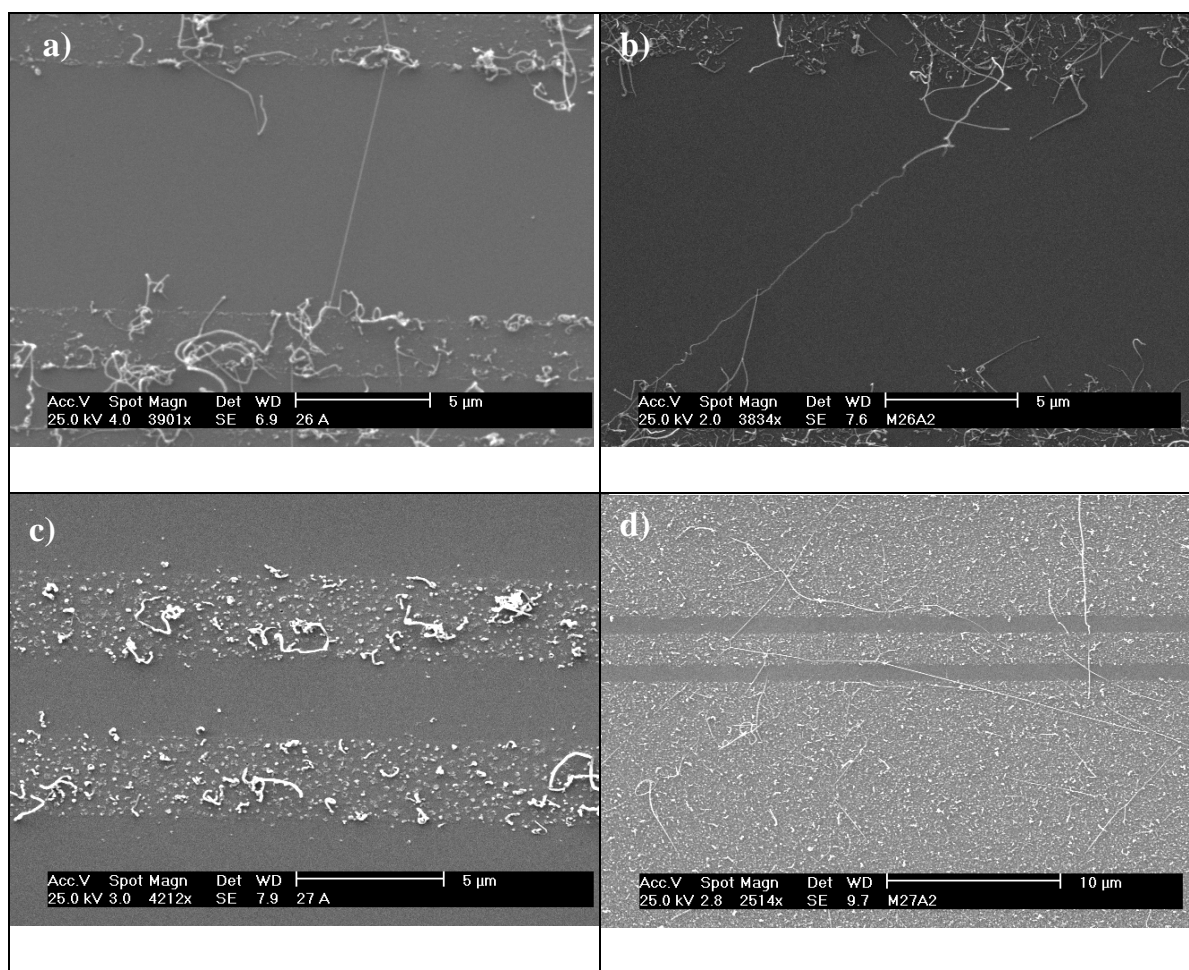


**Fig. 2.3.3**     SEM micrographs of CNTs grown on OxPSi. **a)** Strips of catalyst with nanotube bridge (M26C1, process 1) and **b)** strips of catalyst whit CNTs protruding from the islands (M26C2, process 2). Micrograph of CNTs on SO of **c)** process 1 (M27C1) and **d)** process 2 (M27C2).

Process 1 and 2 differ for the annealing gas. The $H_2$ used in the annealing step of process 2 leads to a quite cleaner surface and it enhances the nanotubes nucleation on SO where no nanotubes grow when argon is used (process 1).

72

In fig. 2.3.4 and 2.3.5 we collect SEM micrographs of different substrates undergone to the deposition process 3. This process differs from the first two for the presence of $H_2$ assisting all the process steps. The SEM micrographs of OxPS sample undergone to the deposition process 3 are shown in fig. 2.3.4. The hydrogen here is used during the annealing step instead of argon to obtain a better fractioning of the catalyst.
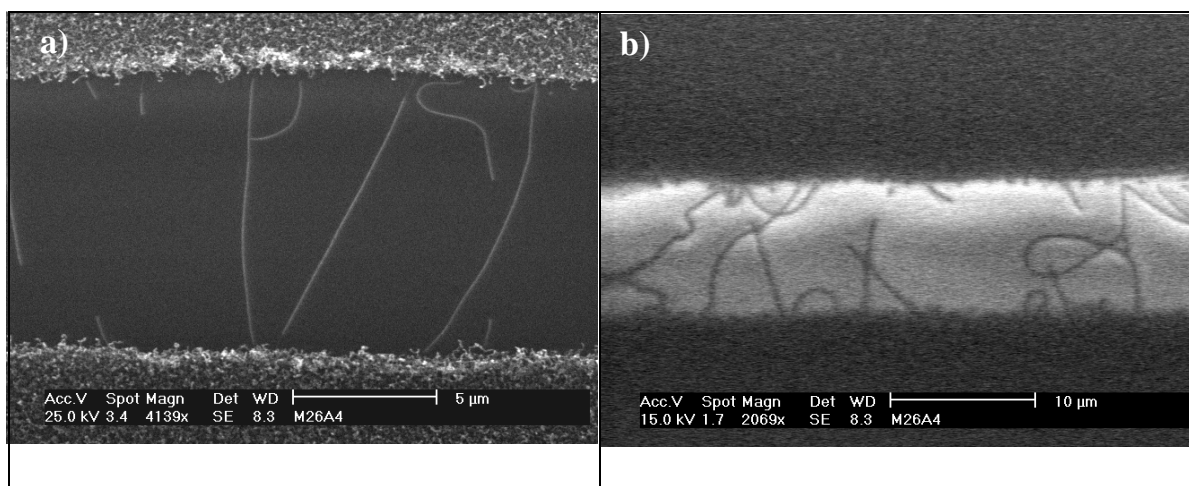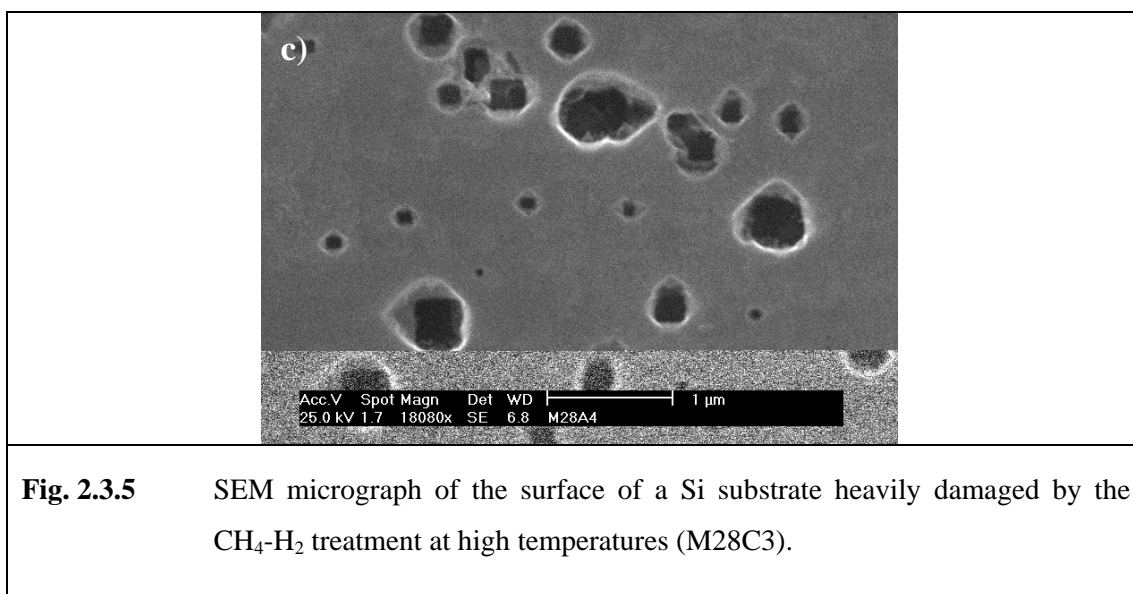


**Fig. 2.3.4**     SEM micrographs of CNTs grown on OxPS (M26C3) with process 3 in **a)** stripes of 2 nm of Fe with nanotube bridging across. **b)** image of the electrons coming from the CNTs collected at a frequency of 50 scan/s.

Process 3 is completely carried out in $H_2$ atmosphere. Here $H_2$ is used both as a carrier gas as well as a co-deposition gas. The main difference among this process and the processes 1 and 2 is in the higher density of nanotubes nucleation from catalytic sites on the strips. CNTs are long enough to bridge across adjacent strips separated of several microns. The CNTs grown in this case are thinner than that shown in the previous processes. Fig. 2.3.4 b) is collected focusing on electrons backscattered from the sample. The dark areas arise from the contribution of electrons from metal patterned stripes and nanotubes.

One of the main characteristic of hydrogen is its higher thermal conductivity with respect to argon and other gases. It is reasonable to consider that because of this property, hydrogen can lead to a higher fractioning of the metal catalyst layer. Moreover, hydrogen also determines a reduction effect, by forming several hydrides. These two observations explain the double role of the hydrogen during the growth. In fact thinnest nanotubes are a consequence of the more effective fractioning of

nanoparticles, while a decrease of carbon impurities over the strips is connected with the reduction effect of the hydrogen.

In fig. 2.3.5 we have reported a SEM micrograph of the S substrate undergone to the deposition process 3.



**Fig. 2.3.5**      SEM micrograph of the surface of a Si substrate heavily damaged by the $CH_4$-$H_2$ treatment at high temperatures (M28C3).

No nanotubes are grown on silicon and the surface appears hardly damaged from the process. Hydrogen is responsible of an unwanted etching process occurring during the deposition step. This etching process heavily damages the silicon surface, opening sub-micrometric holes that arise from a hydrogen induced wash.

We suppose that this anomalous etching of Si is due to hydrogen in combination with methane during the deposition process. To verify this hypothesis, the last process (process 4) was performed in whole methane. In order to preserve its fractioning and reducing effects, avoiding the unwanted etching of silicon, the $H_2$ is used in the annealing, ramp-up and ramp-down steps except for the deposition. A typical result of carbon nanotubes grown with the process 4 on SO substrate is shown in fig. 2.3.6.
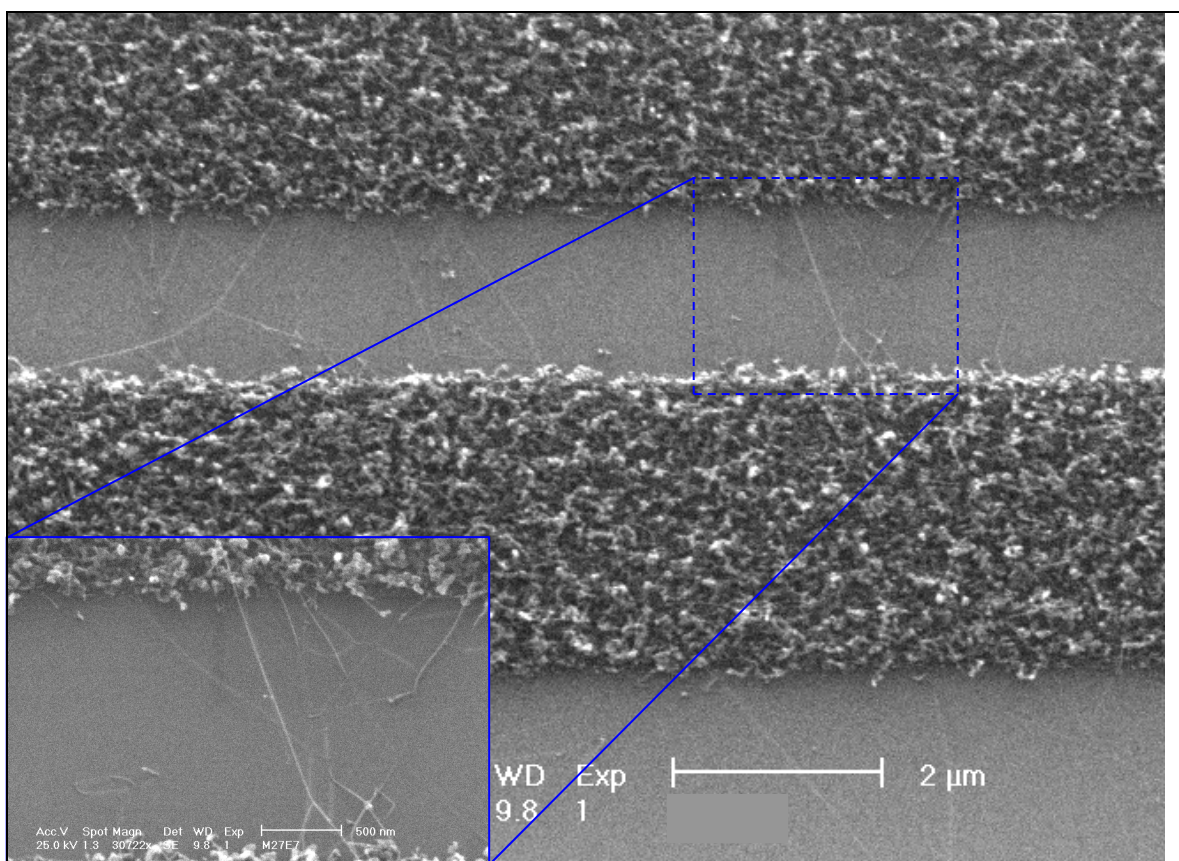
**Fig. 2.3.6**     SEM micrographs of CNTs grown across the strips of 1 nm of evaporated Fe on SO substrate (M27A4). Carbonaceous deposits are visible on the top of the strips.

The sample M27A4 shows very thin carbon nanotubes bridging across Fe stripes and carbonaceous deposits such as nanofilaments and nanoparticles on the top of the stripes where a larger amount of iron is evaporated. This result shows as all the steps toward a more controllable nanotube growth have been preserved passing from process 1 up to process 4. In process 4 all the deposition parameters have been optimized to obtain the best conditions of growth. In particular we have maintained the nanotubes bridging property and the reduced diameter size. In the inset of fig. 2.3.6 a magnification of a Y-type of nanotube bridging across the strips is reported. Moreover the positive effect of $H_2$ treatment on particles fractioning is still valid.

In fig. 2.3.7 we show SEM micrographs of CNTs grown on SO substrates where a film of 2 nm of Fe has been deposited according to the process 4.
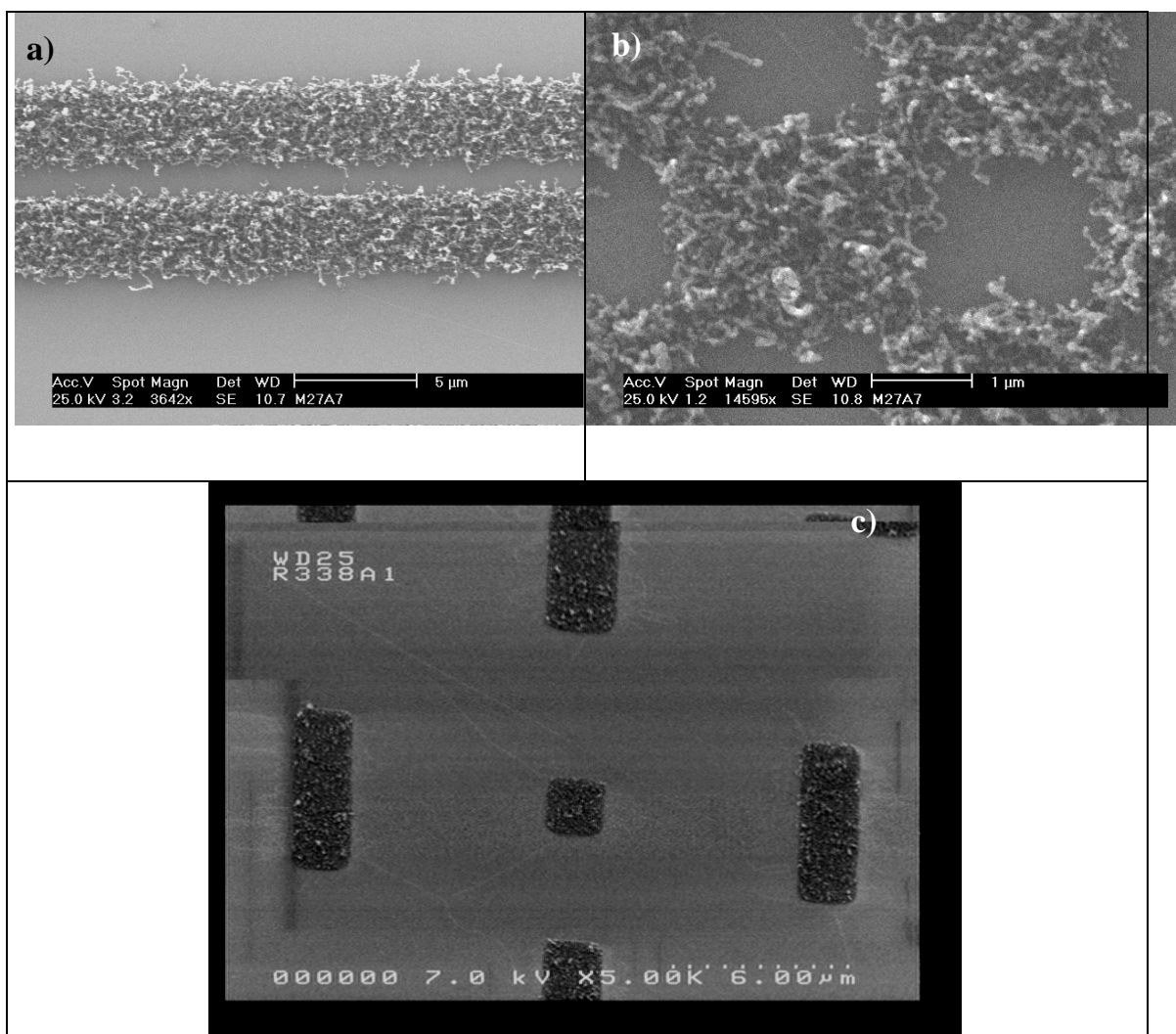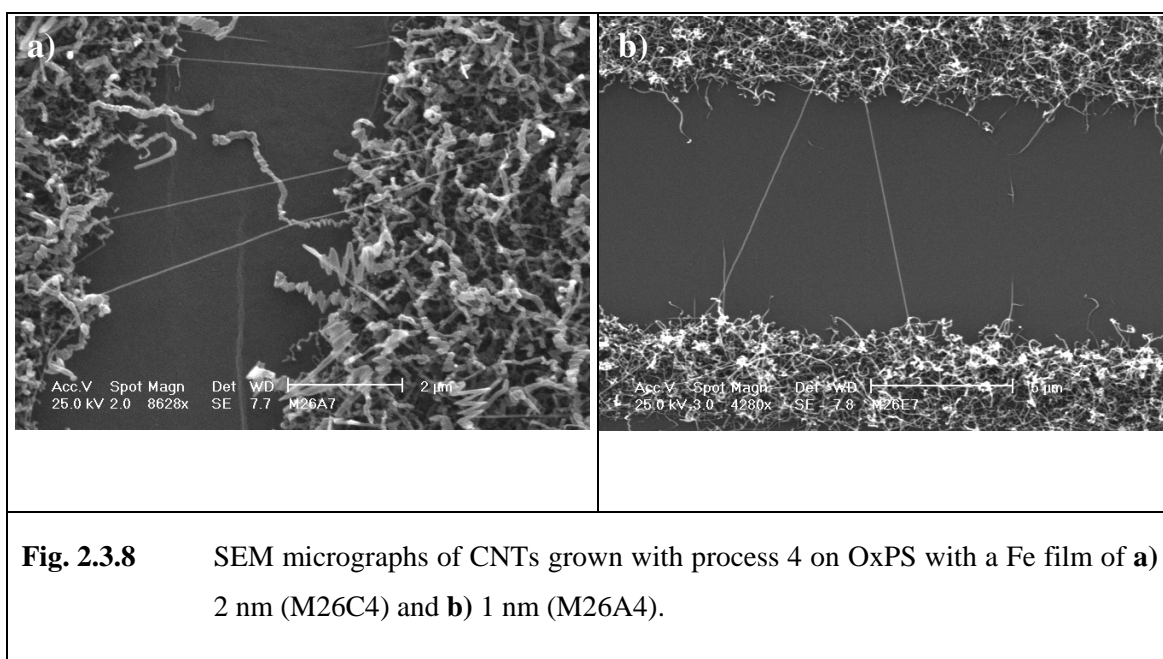
**Fig. 2.3.7**     SEM micrographs of CNTs grown on SO substrates: **a)** strips (M27C4), **b)** squares (M27C4) and **c)** rectangles (R338A4) with a Fe film of 1 nm. The name in the picture of c) micrograph doesn't correspond to the nomenclature established in this paragraph.

These micrographs show as carbon nanotubes bridge between nearest catalyst islands independently from the pattern shape (stripes, squares, rectangles). On the R338A4 sample we observed very long and sometimes coiled CNTs nucleating on the catalyst rectangles and starting from there toward nearest patterned areas. Large distances between catalyst islands don't represent a problem for growing nanotubes that are able to overcome distances up to several microns before stopping their elongation according to the "kite-mechanism" (see Chap.V).

The SEM images reported in fig. 2.3.7 a) and b) show many carbonaceous deposits on the top of patterned stripes and squares. These results, compared with the nanotubes grown on the corresponding SO substrate of fig. 2.3.6 with 1 nm of Fe,

evidence two main differences. The impurities concentration on the patterned catalyst islands is higher for 2 nm thick Fe films than for 1 nm films as can be clearly distinguished comparing fig. 2.3.7 a) and c). No thin and bridging carbon nanotubes are clearly visible on SO with 2 nm of Fe. This allows concluding that films of Fe of 1 nm of thickness are closer to the best condition of thin and bridging nanotubes.

In fig. 2.3.8 SEM micrographs of carbon nanotubes and nanofilaments grown on OxPS with both iron thickness of 1 nm and 2 nm, are reported.



**Fig. 2.3.8**    SEM micrographs of CNTs grown with process 4 on OxPS with a Fe film of **a)** 2 nm (M26C4) and **b)** 1 nm (M26A4).

The process on OxPS substrates with 1 and 2 nm Fe patterned films results both in long CNTs bridging across the strips and in a high density of carbonaceous material as tubes or filaments on the strips. These filaments and deposits could be something similar to the carbon fibers or other kinds of carbon based materials (glassy-carbon, carbon blacks or amorphous carbon) as illustrated in the Appendix D. The nature of these carbonaceous residuals could be clarified only by means of further characterization analysis.

In fig. 2.3.9 we show SEM micrograph of M28A4, a Si substrate with a 1 nm of evaporated Fe on the stripes (process 4).
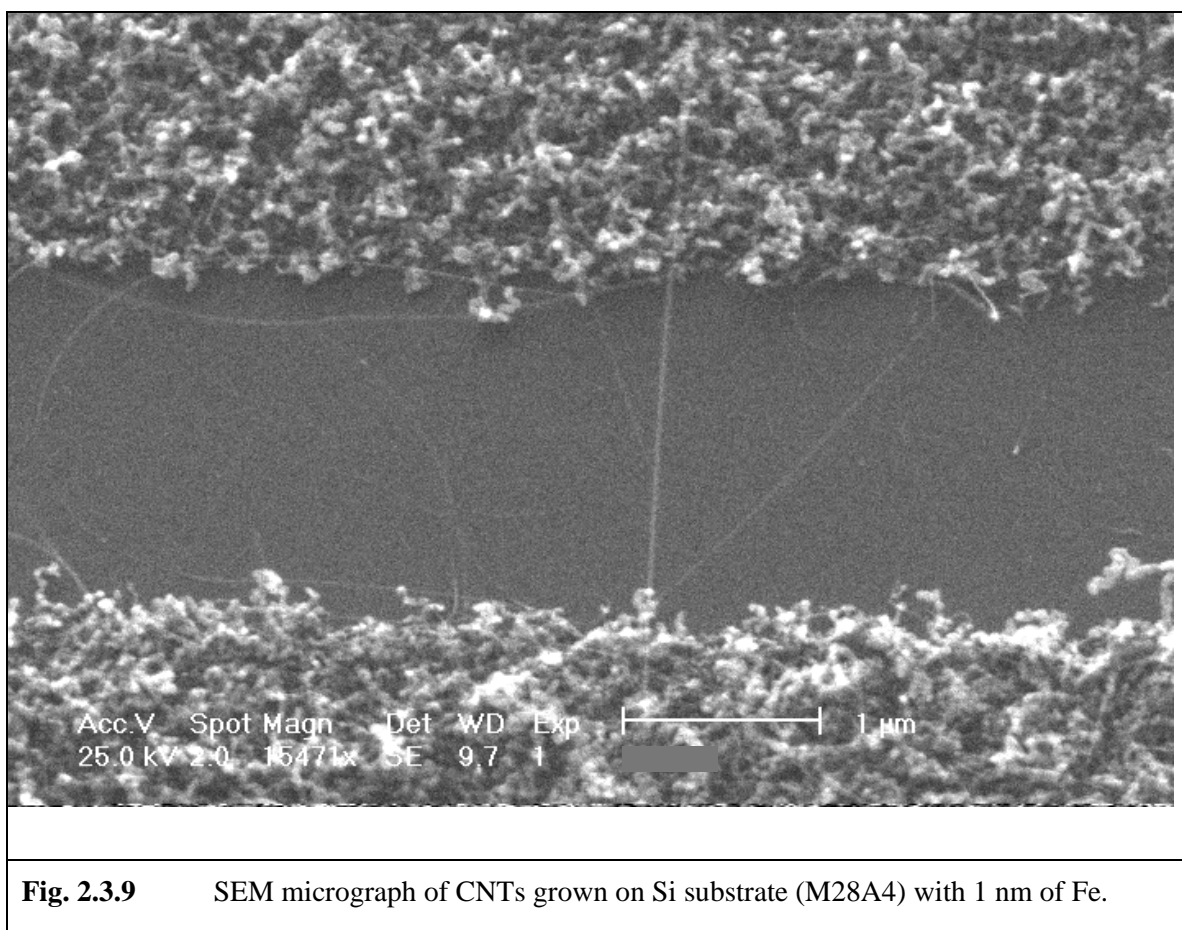
**Fig. 2.3.9**        SEM micrograph of CNTs grown on Si substrate (M28A4) with 1 nm of Fe.

The picture shown in fig. 2.3.9 illustrates as the hypothesis that the unwanted Si etching was due to the combination of methane and hydrogen during the deposition step, was correct. The sample in fig. 2.3.9 is very different from the silicon sample shown in fig. 2.3.5. Process 4 in pure methane, does not damage the S substrate by an unwanted $H_2$ etching, leading at the same time, to site selective nanotube nucleation. This means that the hydrogen erosion effect is due to the methane-$H_2$ combination at 900 ºC. For the general purpose of the implementation of industrial scalable processes it is fundamental to achieve good deposition growth on silicon substrates.

### 2.3.4 Summary

In the following we point out some differences occurring for the CNTs growth on these types of substrates with respect to the growth processes reviewed in the paragraph 2.2 (dots of silicon and porous silicon).

The main difference between the *forest-like growth* and the resist *patterned growth* results is connected with the substitution of acetylene with methane. This gas

decomposes at higher temperatures compatibly with the conditions for SWNTs nucleation and growth. The higher decomposition temperature of methane along with the use of hydrogen reduces the probability of depositing amorphous carbon with respect to the case of acetylene. In this respect, methane can be considered as a cleaner hydrocarbon for the deposition processes of carbon nanotubes. This is clearly a gaining factor in order to achieve the controlled growth of CNTs on microelectronic devices.

- Another difference is connected with the reduction of the thickness of the catalyst layer as well as of the amount of catalyst material in each island. We reduced the Fe thickness to 1 and 2 nm thick films. This thickness reduction enables the formation of smaller nanoparticles and a higher density of nucleation sites, thus leading to the nucleation of nanotubes of smaller diameters. In fact, there's a correlation between the size of the metal nanoparticles and the nanotubes nucleation process. The smaller the size of the nanoparticle the higher is the probability to have the nucleation of the carbon nanotube. Moreover, there's also a correlation between the diameters of the grown nanotubes and the diameter of the nanoparticles. The smallest nanotubes can be grown from very small catalyst nanoparticles [6].

- The third difference is the localization of the catalyst in small patterned areas (strips, squares...) $\mu$m wide. CNTs resulting in this case are well localized on Fe islands, eventually protruding from them to bridge across the strips and squares. This is a property that can be very helpful in order to achieve our goal: the localized growth of single nanotubes.

- In the growth performed using methane atmosphere and micropatterned islands, we observe a shift from a vertical, highly dense growth to a horizontal and sparse CNTs growth. In this case the CNTs are both short and located on the strips or long and bridging between adjacent patterned islands. This is an interesting point to be further investigated.

In conclusion, we defined a standard deposition process working well with all the substrates of interest (e.g. Si, $SiO_2$, OxPS), leading to thin nanotubes nucleated in well defined positions on the wafer and forming bridges across strips and squares.

## *2.4 Growth of Carbon Nanotubes on trench patterned substrates: Self - bridging of CNTs*

Until now we have demonstrated as a set of micropatterned strips of a catalyst can localize the growth of carbon nanotubes onto the strips giving rise to a bridging effect between adjacent strips. Because of the interest connected with such a phenomenon it is worth to investigate the existence of substrates or conditions that can determine an enhancement of the bridging effect. In fact, the integration of carbon nanotubes in electronic devices requires the localization of the growth and the control of the orientation in order to make easier the localization of the electrodes.

In this section, we will investigate how the substrate morphology can influence the growth of carbon nanotubes. We show that by using a particular pattern it is possible to orient the growth and align the carbon nanotubes. We are mainly interested in the study of self bridging properties of nanotubes across spaced 3D structures and in the correlation between substrate properties and CNTs nucleation and growth.

In particular, three different kinds of substrates consisting of silicon (S), silicon oxide (SO) and poly silicon (poly-Si) were patterned by using a standard lithographic and anisotropic etching process with a set of parallel trench structures. The trenches have sub-micrometric dimensions and they are used to test if the horizontal, well located CNTs growth, already obtained in the group of samples with patterned catalyst, is still preserved. As a fact, the patterned trench-structures introduce a periodic set of physical embossed strips that the growing nanotubes have to overcome. As a result, we expect that suspended bridge structures of CNTs can connect adjacent rows. Moreover we also tested the effects of standard surface chemical treatments, in use in the microelectronic industry, on the nucleation and growth steps.

Si, SO and poly-Si patterned trench substrates were covered with thin Fe films, both by e-gun evaporation as well as by dip or spin coating technique starting from a salt solution containing the metal catalyst precursor ($Fe(NO_3) \cdot 9H_2O$). The second method was used in order to gain a finest control on the size and dispersion of the iron nanoparticles (Fe-NPs).

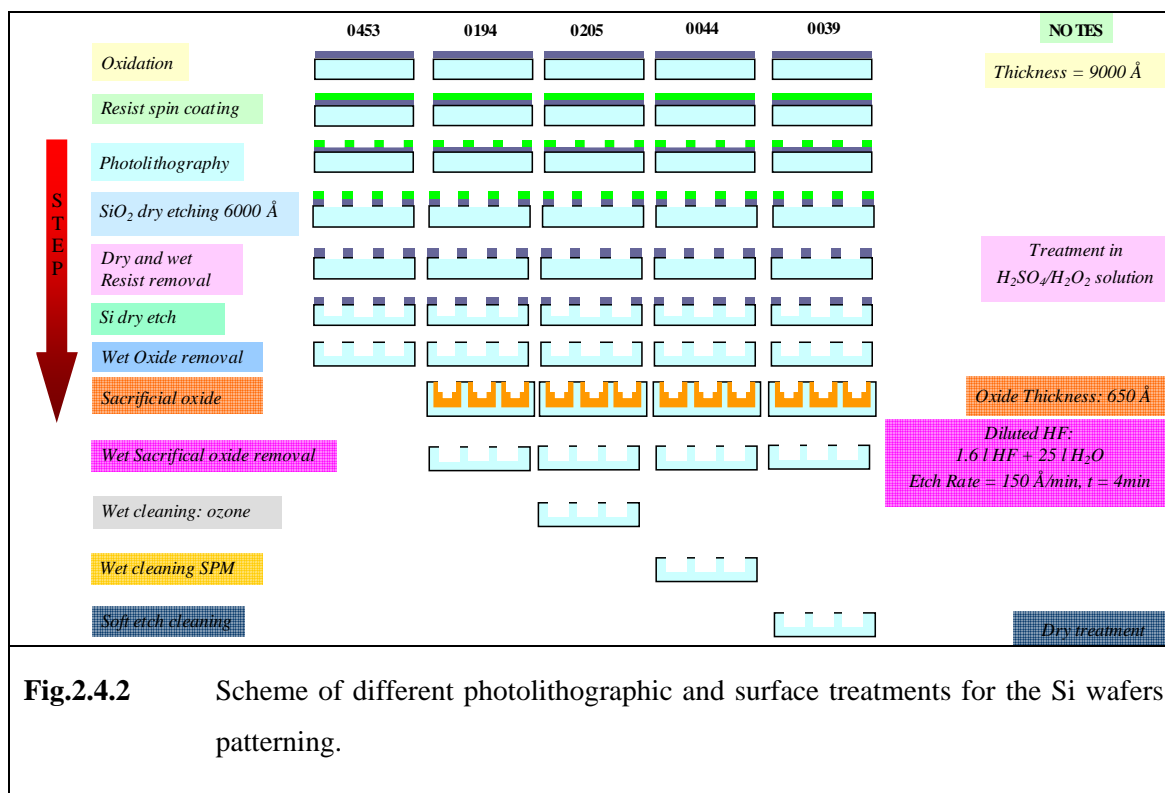### *2.4.1 Substrates selection and metal catalyst coating*

As stated above three types of substrates were selected in order to study the influence of the morphology of the substrates on the growth of carbon nanotubes: they were Si, SO and Poly Silicon (Poly1 and Poly2) where trench patterns defined by standard optical lithographic techniques were obtained. Moreover, the S and SO wafers received different surface treatments to test the effect of a chemical surface handling on CNTs growth. A simple scheme of SO preparation steps is sketched in fig. 2.4.1. The number on the top of each column is the wafer identification number corresponding to a particular surface treatment.



**Fig.2.4.1**    Scheme of different photolithographic and surface treatments of SO wafers.
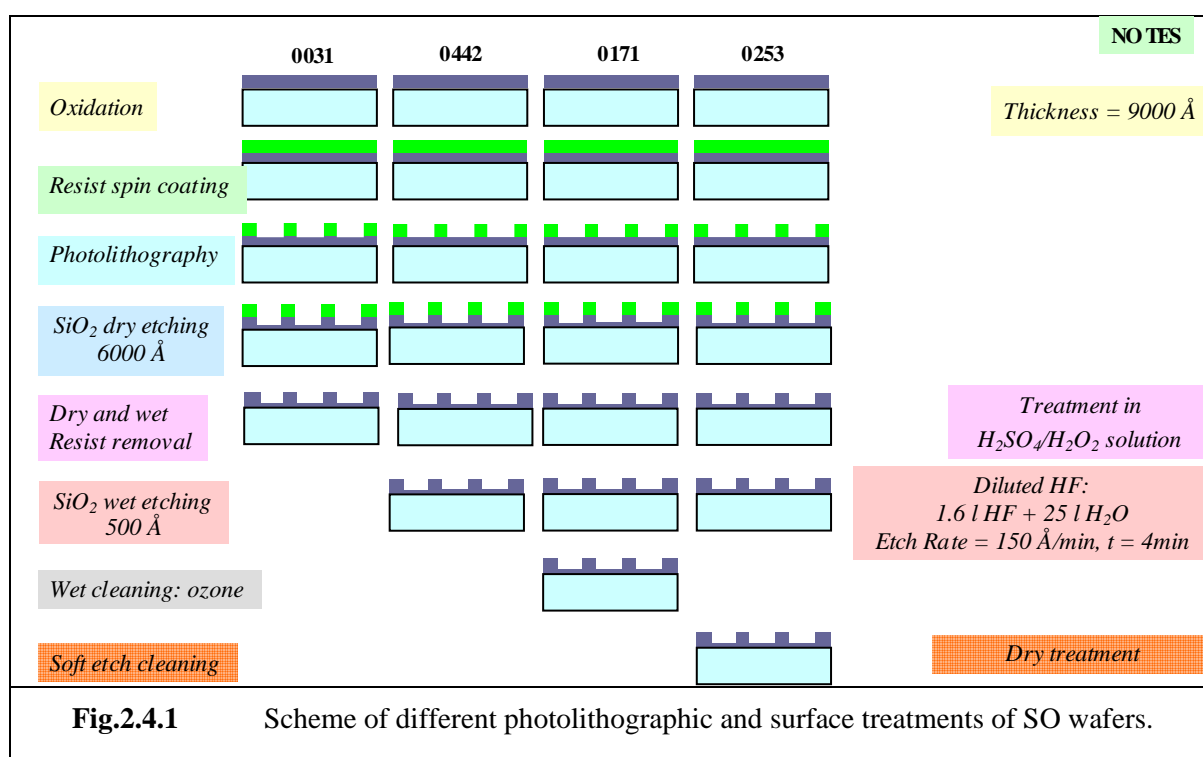
In particular, all the SO substrates underwent a thermal oxidation step aimed to obtain a layer of thermal silicon oxide 9000 Å thick. Then a resist layer is deposited on the top of the SO substrate and windows, giving the desired trench pattern, were opened and transferred on the wafer after a canonical photolithographic step. Subsequently, a dry etching is performed on the resist patterned $SiO_2$ surface in order to remove an oxide layer of about 6000 Å, leaving a SO surface with a high roughness. This gives rise to the trench-structure. The following step implies the resist removal that is further followed by a wet etching in a diluted HF solution which is intended to remove 500 Å of SO and smooth the surface. The 0031 SO wafer didn't

undergo to this HF smoothing step. After this step the substrates differ each other for the cleaning treatment. The 0071 and 00253 wafers underwent, respectively, to a wet cleaning treatment in ozone and a soft etching treatment in order to modify the substrate roughness.

A similar procedure is used to obtain the trench patterns on Si wafers (the main steps are reported in fig 2.4.2). The set of masks here used is the same as for SO samples, but a further group of steps is introduced. In fact, in the case of Si, a supplementary sacrificial oxide layer is introduced to obtain an anisotropic etching of the silicon surface that leaves well defined trenches, avoiding the rounding up of the trenches sides (see fig. 2.4.3).



**Fig.2.4.2**     Scheme of different photolithographic and surface treatments for the Si wafers patterning.
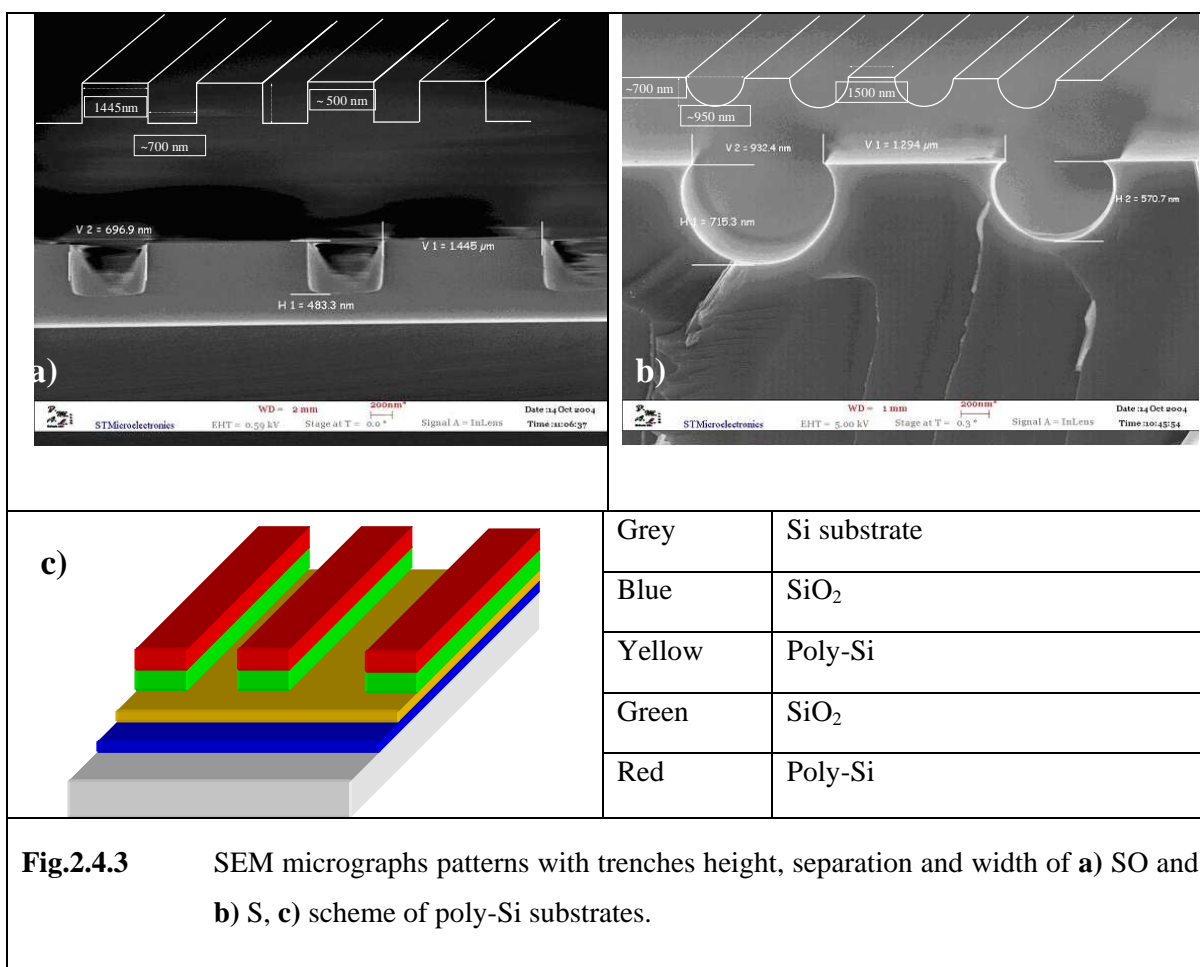
In particular, the steps for the Si and the SO patterning remain unchanged up to the dry and wet resist removal. After these steps a dry etching is performed, followed by the oxide layer removal that leaves the Si surface exposed to the etching process. The next step is the formation of a sacrificial oxide layer to obtain the anisotropic S etching. SO layer formed of about 65 nm is then removed with a wet process in a diluted HF solution. As previously, the wafers are distinguished by their code that marks a different subsequent treatment of the surface. In particular, the 0453 wafer

doesn't undergo to the oxide sacrificial layer deposition, whereas the 0194 wafer is obtained after the sacrificial oxide removal. The difference between 0205, 0044 and 0039 is in the cleaning process of the surface.

Poly-Si substrates Poly1 and Poly2 show the same trench geometries but with different dimensions of the trenches. They have been obtained using the same lithographic steps used for S39 wafers.

The patterned trenches of SO are about 1.5 µm wide, 0.5 µm high and spaced of about 0.7 µm. The corresponding dimensions of Si trenches are $1.3 \, \mu m \times 0.7 \, \mu m \times 0.9 \, \mu m$. The spacing, width and height of Si and $SiO_2$ trenches have been determined during the SEM image acquisition and the precise values are reported on the cross section images of these samples in fig. 2.4.3 a) and b). $SiO_2$ is usually etched by Reactive Ion Etching (RIE) using $SF_6/CHF_3/He$ etch gas mixture. This process results in the squared profile of the oxide with vertical sidewalls. The fluorine atoms from $SF_6$ quickly etch the oxide, while the $CHF_3$ concurrently creates sidewall polymers. The profile angle is determined by the quantity of $CHF_3$. On the other hand, Si is usually etched by RIE using a different etch mixture, solely $SF_6$. This results in an isotropic etching. A $Cl_2/HBr$ mixture would be necessary to obtain anisotropic etching, with the possibility of obtaining quite vertical sidewalls (profile angle = 88°/90°). However, this facility is not present in the development line of STMicroelectronics in Catania.

| Grey | Si substrate |
|------|------|
| Blue | SiO$_2$ |
| Yellow | Poly-Si |
| Green | SiO$_2$ |
| Red | Poly-Si |

**Fig.2.4.3**     SEM micrographs patterns with trenches height, separation and width of **a)** SO and **b)** S, **c)** scheme of poly-Si substrates.

In fig. 2.4.3 c) a sketch of the poly-Si substrates is reported. The trenches patterned on poly-Si have been produced with two different spacing, one about 2 µm wide (Poly1 broader trenches) and the other one about 5 µm wide (Poly2 narrower trenches). The use of substrates commonly adopted in the microelectronic industry is a key feature in order to gain a rapid integration of new materials in the flowchart process of the traditional semiconductor ultra large scale integration. Therefore, all these patterned substrates have been here employed to test the ability of nanotubes to self-arrange by bridging across two or more trenches.

We will report the remarkable examples of CNTs growth on Si, Silicon oxide and poly silicon trench patterned structures, after catalyst deposition. The effect of surface treatment has been also analyzed.

In the previous section we considered extensively the evaporation method in order to deposit the iron catalyst on the substrate surface. In this section we will continue to use the evaporated films as a source for the metal nanoparticles.

Nevertheless, because of the intrinsic limit of the evaporation an accurate control of the catalyst thickness below 1nm is not possible. As a consequence, we considered other methods. We implemented the use of iron nitrate salt solution in isopropyl alcohol in order to have a very accurate control on the amount of catalyst.

The salt used is a iron nitrate 9-hydrate ($Fe(NO_3)_3 \cdot 9H_2O$ (403.9 as a molecular mass). It is a metal precursor containing the catalyst active for the nanotubes synthesis. The salt is dissolved in isopropyl alcohol to obtain a solution of the desired concentration (0.4 mM). After adding the isopropyl alcohol to the salt, the solution is magnetically stirred for a long time to enhance the nanoparticles formation. We start our experiments with highly diluted salt solutions because one of the aims of this work is the control over CNTs density, alignment and diameter size. The ability to control metal-NPs size yields to the growth of nanotubes of the desired diameters. The chemical procedure allows to obtain an efficient catalyst fractioning and spreading providing synthesized nanotubes with small size dispersion.

The liquid isopropyl alcohol solution of iron nitrate determines a certain solubility of the iron salt that, as a general fact, is lower than that of water (the iron solution must be maintained stirred for a long time). It is likely that, this liquid solution produces suspended small clusters of iron nitrate that could give easily rise to small Fe-NPs once the solution is deposited on the substrate. In fact, the isopropyl alcohol quickly evaporates leaving dispersed Fe-NPs on the substrate. During the growth process the high temperatures involved guarantee the nitrate evaporation thus leaving pure metal Fe nanoparticles distributed on the substrate. The deposition can be achieved by using two methods: the spin (SC) and the dip coating (DC) procedure. The spin coating consists in a quite homogeneous coating of the sample with a well defined quantity of salt solution, dispersed by means of a spin coater. After the dispersion, samples are annealed in air at 80 °C for 10 minutes. The dip coating consists in the immersion of the samples on the bottom of a beaker containing a defined amount of the solution. After this immersion, samples are left drying in air under a hood.

The e-gun evaporation (A), spin coating (B) and dip coating (E) processes for the catalyst coating are summarized in the table 2.8. D and B processes only differ for the number of spinning cycles.

| Deposition Process | Name | Deposition Parameters | Samples |
|---|---|---|---|
| e-gun evaporation | A | 1 nm , 5 Å/s, 2 s | S39A <br> SO253A <br> Poly1A <br> Poly2A |
| Spin Coating | B <br> *Repetition time* <br> 1 | *Solution Quantity* <br> 500 µl of sol. <br><br> *Spinner settings* <br> 500 rpm, t = 5 s | S39B <br> S453B <br> SO31B <br> SO253B <br> Poly1B <br> Poly2B |
| | D <br> *Repetition time* <br> 2 | *Oven Settings* <br> T = 80 °C t = 600 s | |
| Dip Coating | E | *Features of the immersion* <br> 200 ml of sol. for t = 4h | SO253E <br> Poly1E <br> Poly2E |

**Table 2.8:**     Catalyst deposition processes used for the trench structures: main deposition parameters of the three catalyst deposition processes and type of samples used for the *self - bridging* CNTs growth.

The substrates coated with 1 nm of evaporated Fe or with metal-NPs from solution, undergo the deposition processes described in the following section.

## 2.4.2 Chemical Vapor Deposition of Carbon Nanotubes on trench-patterned substrates

In the previous section we argued that the best deposition process was that labeled as process number 4 (see table 2.7), performed by using hydrogen in the ramp-up and ramp-down as well as in the annealing steps with the exception of the deposition process, that is pursued in a pure $CH_4$ atmosphere. Therefore, process 4 of

table 2.7, optimized on the substrates used up to now, was also used on the trench patterned substrates. The synthesis step is carried out in pure methane in the tube quartz furnace (for the deposition steps to refer to the table 2.7). The process flowchart described in this table will be used in the following also in the device growth section because this is actually the best process we developed in the tube quartz furnace compatible with CNTs growth on substrates commonly used in the microelectronic industry. The samples were unloaded and their morphology analyzed by the SEM.

### 2.4.3 SEM characterization of as-grown samples

Samples inspection and structural analysis was achieved by using the SEM technique. In fig. 2.4.4 the SEM micrograph of the S39A sample with 1 nm of evaporated Fe is shown. This sample is a silicon substrate, particularly interesting for the surprising preferential orientation of carbon nanotubes bridging across trenches. In fig. 2.4.5 a magnification of the well defined area (blue dashed rectangle) of the S39A SEM image of fig. 2.4.4 is displayed.
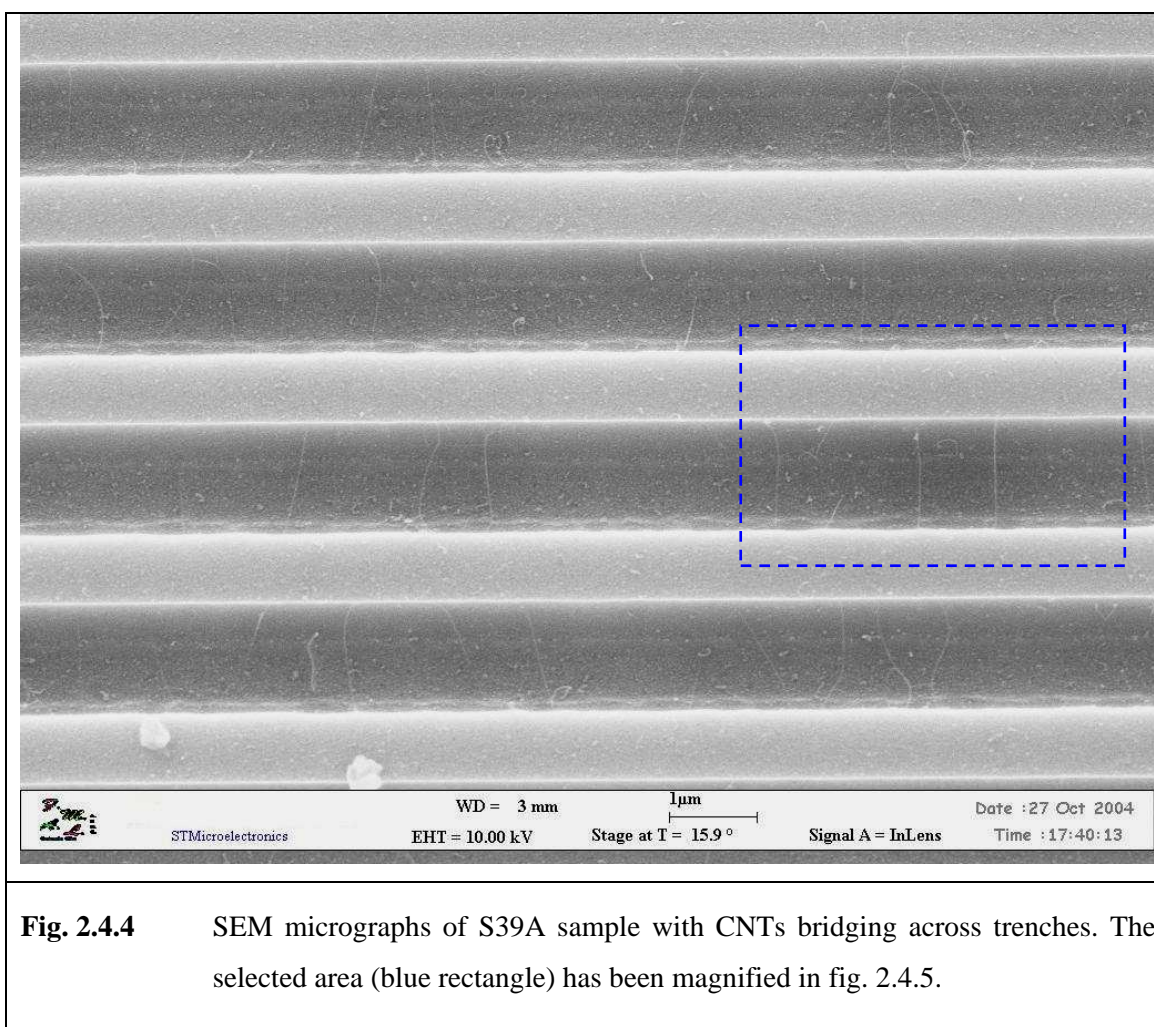
**Fig. 2.4.4**     SEM micrographs of S39A sample with CNTs bridging across trenches. The selected area (blue rectangle) has been magnified in fig. 2.4.5.

Using the Fe evaporation process A on silicon substrates, a sparse network of suspended CNTs with a well defined direction had been achieved. The nanotubes nucleation occurs at the edges of trenches, as shown in fig. 2.4.5. The nanotubes grow horizontally, perpendicularly to the trench sides with almost no nanotubes on the bottom and on the top of trenches. The catalyst is spread everywhere on the surface but no carbonaceous deposits are visible. This result is original with respect to the kind of nanotube growths achieved in the previous section.
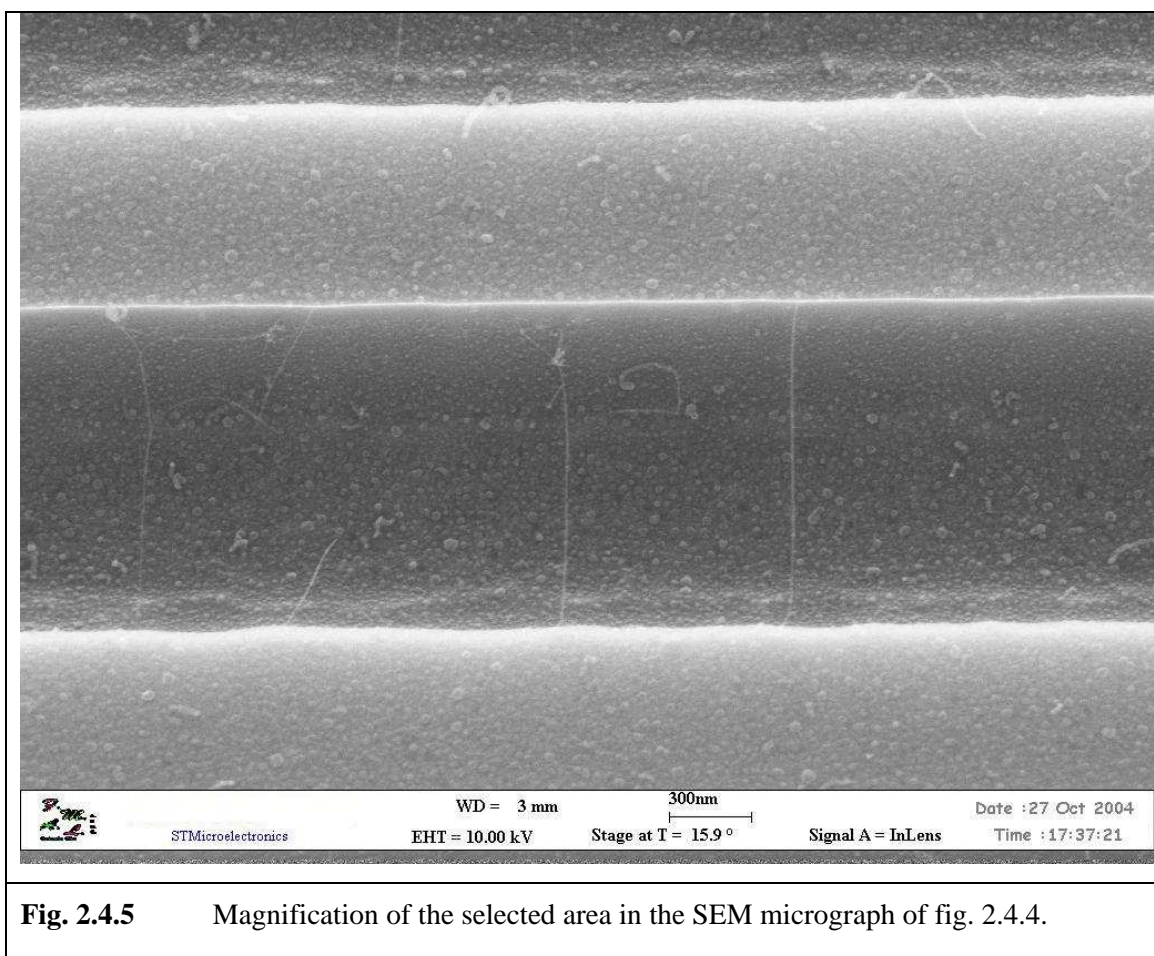
|  |  |
|---|---|
| WD = 3 mm | 300nm |
| EHT = 10.00 kV | Stage at T = 15.9° | Signal A = InLens |
| STMicroelectronics | | Date :27 Oct 2004 Time :17:37:21 |

**Fig. 2.4.5**     Magnification of the selected area in the SEM micrograph of fig. 2.4.4.

This growth process provides better results with respect to the group of carbon nanotubes grown on micropatterned substrates. In particular, we can observe that the substrate surface is clean from deposits and the bridging carbon nanotubes are very thin, showing a low density. The mean number of bridging nanotubes is about $32 / 119\ \mu m^2$, meaning that a concentration of about 1 CNT / 4 $\mu m^2$ has been achieved. The round drops visible on the top and at the bottom of trenches are the Fe-NPs arising from the 1 nm thick Fe film. The CNTs on this sample appear starting forming bridges from the top of the upper part of the trenches, at their edges.

In order to see if this deposition process provides the same good results on different substrates, we show the SEM micrographs taken on sample SO253A (fig. 2.4.6 and fig. 2.4.7). This sample is the oxide substrate prepared following the higher number of surface treatments before the deposition process, as well as the S39A sample (see figs. 2.4.1 and 2.4.2). This allows making a comparison between S and SO substrates undergone to the same catalyst and deposition processes.
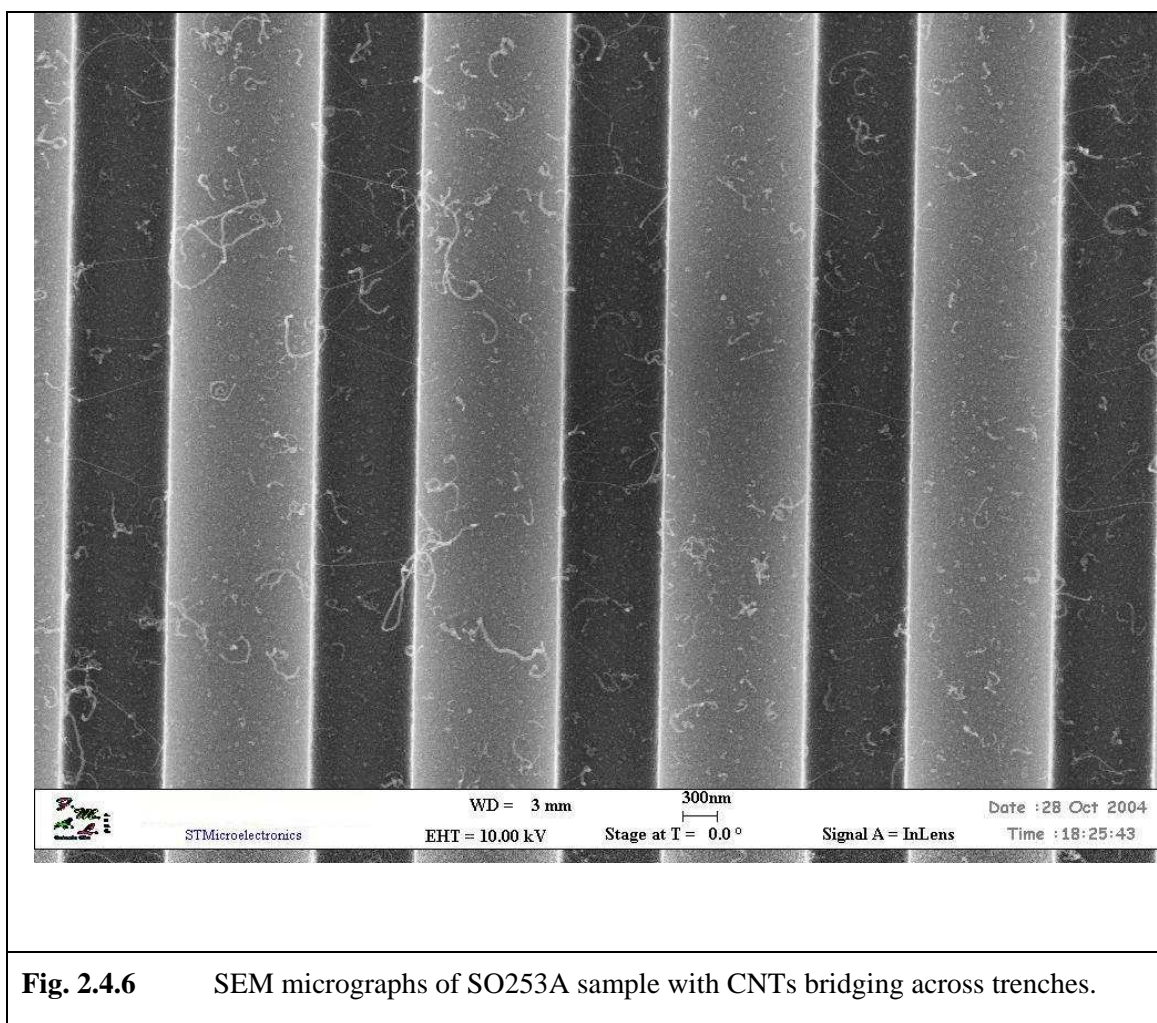
**Fig. 2.4.6**        SEM micrographs of SO253A sample with CNTs bridging across trenches.

The dark rows of figs. 2.4.4 - 2.4.6 are the bottom part of the trenches while the bright strips are the upper part. We can see from SEM image as very thin nanotubes appear bridging across trenches starting from their sides such as for the S39A sample. The SO253A sample shows that many nanotubes in an embryonic phase started to nucleate on the top and at the bottom of trenches. They appear to have larger diameters and a twisted and coiled morphology while bridging CNTs are long, very thin and sparse. The mean number of bridging nanotubes for this sample is about 29 / 67 $\mu m^2$, meaning that a concentration of about 1 CNT / 2 $\mu m^2$ has been achieved. The density of carbon nanotubes bridging across trenches for the SO253A sample is higher than that of S39A sample. This different CNTs density in S and SO substrates is related to the iron silicides and silicates formation. These silicides-silicate iron compounds form when a metal layer is deposited on top of silicon substrates. The phenomenon consists in a chemical reaction between Fe-S-O leading to the formation of Fe stable compounds that disable the catalytic role of Fe. The event of formation of

these stable Fe-Si-O compounds is enhanced by the high temperatures of CVD process and this is the reason why the number of catalytic Fe sites may be reduced on Si with respect to that on $SiO_2$.

The silicidation of iron catalyst occurs especially for small nanoparticles and it is proved that such effect is typical of Si substrates while it is not observed for $SiO_2$ substrates [3]. Fig. 2.4.7 is a SEM micrograph showing a cross section of SO253A sample.



**Fig.2.4.7**      SEM micrographs of a cross section of SO253A sample with CNTs on the trenches.
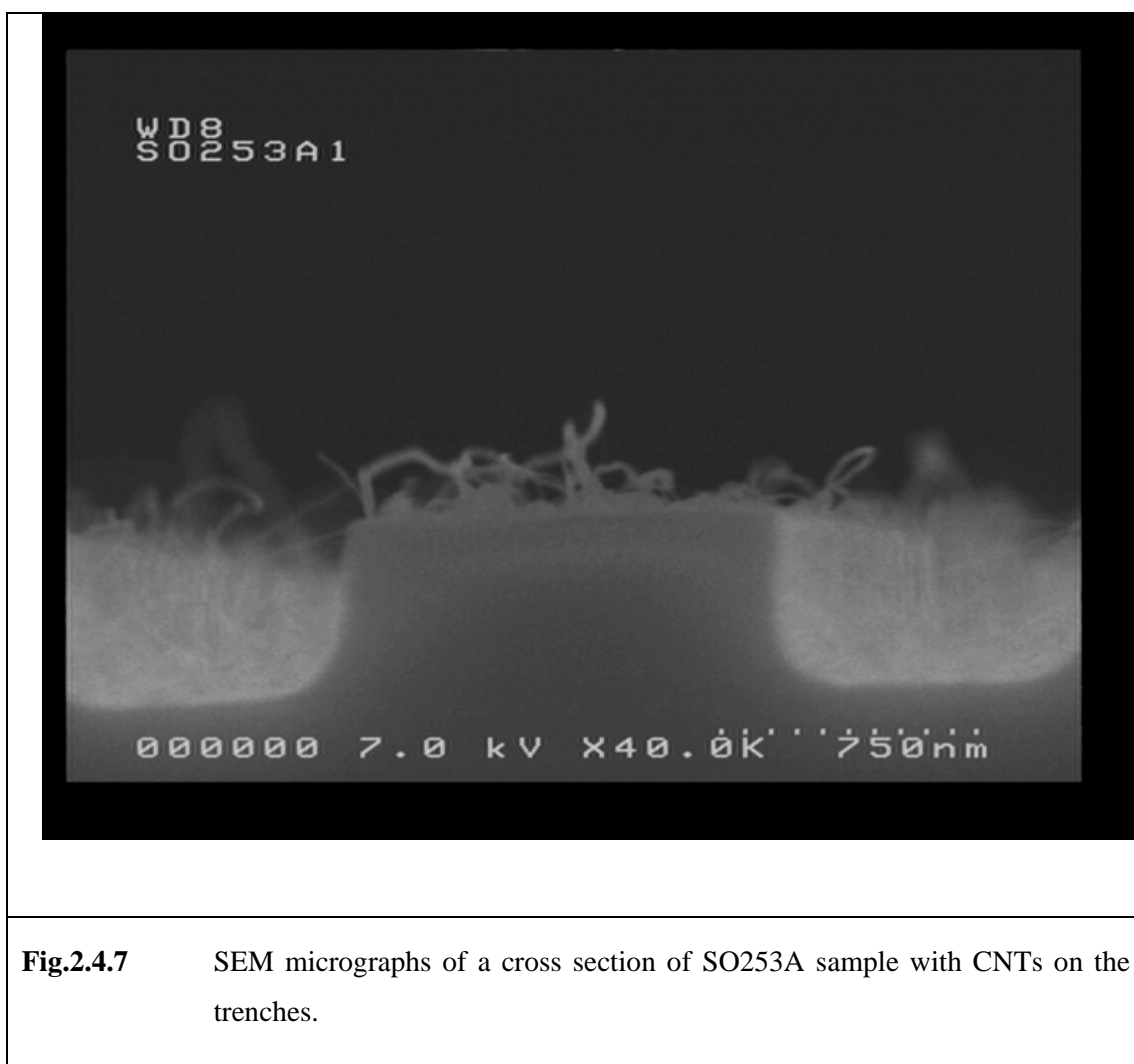
On SO substrate with evaporated Fe, it is possible to observe CNTs grown on the top and at the bottom of trenches as well as tubes bridging across trenches. Unbridging nanotubes strongly interact with the substrate stopping their elongation before reaching the opposite edge of the trench. This leads to the formation of short vertical nanotubes on the top and at the bottom of trenches. The nanotubes bridging

across the trenches are thinner and weakly interacting with substrate during the growth, as suggested by the "kite mechanism" (see Chap.V).

In fig. 2.4.8 we have reported a SEM micrograph of SO253E3 sample. This sample represents an extraordinary example of very thin and long nanotubes bridging across the trenches. The Fe-NPs have been dispersed on the trenches by means of dip-coating of a suitable amount of Fe-salt solution.
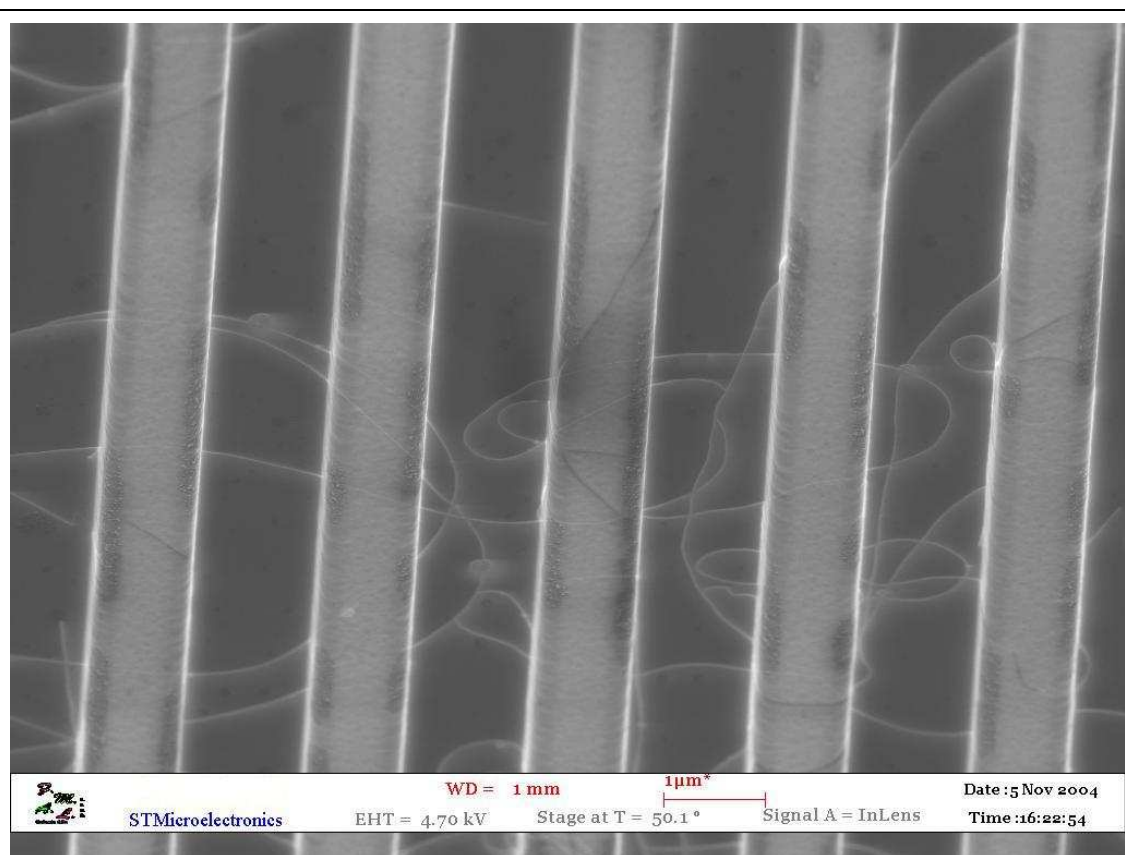


**Fig.2.4.8**      SEM micrographs of SO253E sample with CNTs bridging across trenches.

The SEM micrograph in fig. 2.4.8 shows as the dip coated sample of silicon oxide leads to the nucleation of nanotubes with different morphology with respect to the evaporated samples. With this type of Fe deposition, longer and thinner nanotubes on the top of trenches are produced. CNTs appear to have very small diameters and they are so long to bridge various close trenches. If we keep attention we can observe as round patches of catalyst are clearly visible on the top of trenches. These islands contain Fe-NPs arising from the fast solvent evaporation. This could be explained supposing that, with this procedure, uniform and small Fe-NPs are formed and, as a

consequence, long nanotubes with a small dispersion in size are grown. In fig. 2.4.9 a high magnification SEM image of the same SO253E sample is reported.
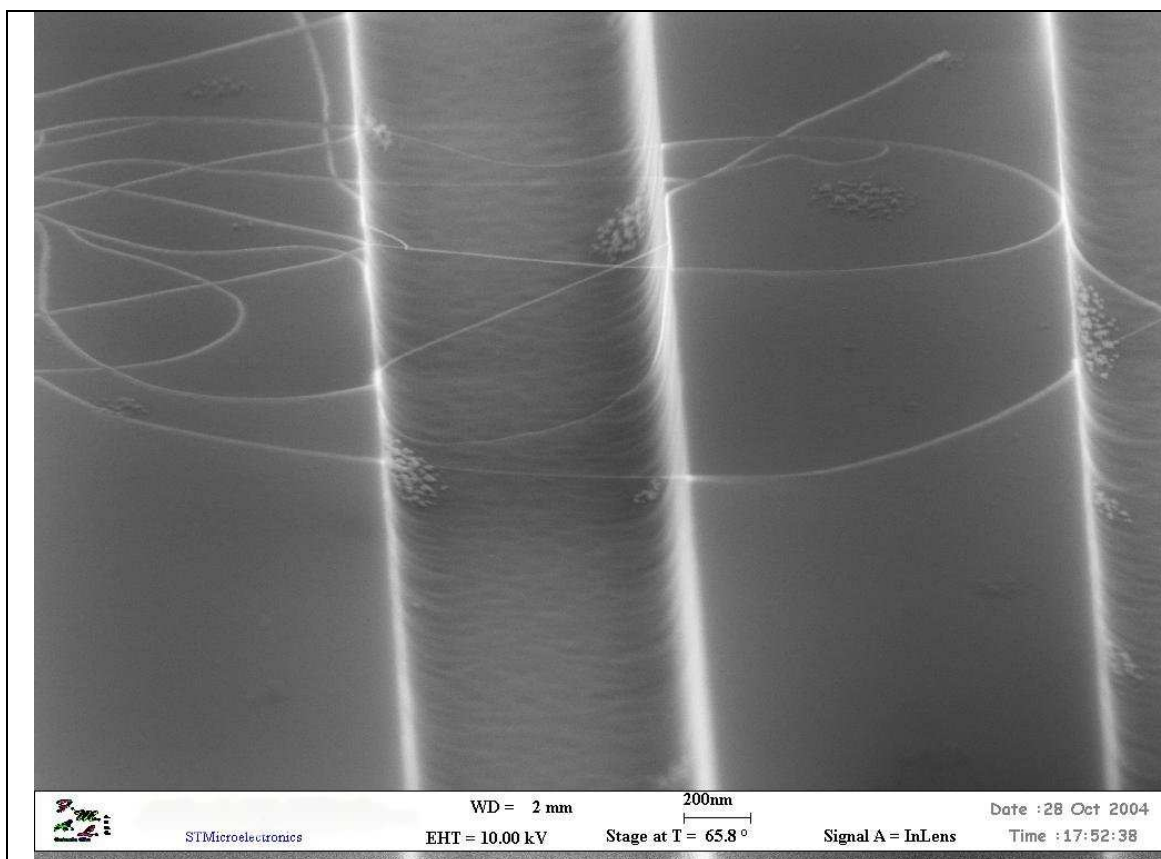


| **Fig. 2.4.9** | SEM micrographs at high magnification of SO253E sample, with CNTs bridging across trenches. |

Carbon nanotubes in this sample appear similar to "cotton thread", lay down on the substrate. We can distinguish as the above-mentioned patches are composed of Fe-NPs located also on the bottom of the trenches, at its edge angles. Therefore, we can conclude that Fe immersion give random bridging of CNTs that are very long and with a lower density with respect to the evaporation process. This could be explained by supposing that with a chemical procedure, uniform and small Fe-NPs are formed and, as a consequence, long nanotubes with a small dispersion in size are grown. In figs. 2.4.10

```
ERROR: typecheck
OFFENDING COMMAND: begin

STACK:

[66 56 100 0 ]
( the)
```